NUMERICAL ANALYSIS OF THE FILM COOLING EFFECTIVENESS ON A HIGHLY LOADED LOW PRESSURE TURBINE BLADE IN CONJUNCTION WITH ENDWALL EFFECTS

A Thesis

by

TYLER GRANT RICE

Submitted to the Office of Graduate and Professional Studies of
Texas A&M University
in partial fulfillment of the requirements for the degree of

MASTER OF SCIENCE

Chair of Committee,	Meinhard T. Schobeiri
Committee Members,	Nagamangala.K. Anand
	Theofanis Strouboulis
Head of Department,	Andreas A. Polycarpou

May 2017

Major Subject: Mechanical Engineering

Copyright 2017 Tyler Rice

ABSTRACT

This thesis is a numerical investigation of the flow development of film coolant injected from a turbine blade with considerations to the effects of the passage vortex. By studying the film cooling effectiveness of a low pressure turbine blade subjected to film cooling parameters such as the compound angle injection, Density Ratio, and Blowing Ratio are varied to understand the impact that these parameters have on the passage vortex and film cooling effectiveness in the near endwall region where the passage vortex effects are most prominent. Film Cooling is important in this region as the passage vortex region of a blade is susceptible to high heat transfer and thermal stresses, which can greatly reduce the life cycle of a turbine blade.

For this study, a special blade was designed that has a total of 605 holes distributed along 13 different rows on the blade surfaces. 6 rows cover the suction side, 6 other rows cover the pressure side and one last row feeds the leading edge. There are six coolant cavities inside the blade. Each cavity is connected to one row on either sides of the blade, except for the closest cavity to leading edge since it is connected to the leading edge row as well. By using ANSYS CFX, a RANS based solver as a computational platform, the study first compared to an experimental benchmark to understand the deficiencies of the numerical simulation, in that the velocity fluctuations were over-predicted in the boundary layer, thus effecting the prediction of mass, momentum, and energy transport. Secondly, in varying the different parameters the interaction of the film cooling vortices and passage vortex is studied. The development of the film cooling

vortices with varying parameters and the effects due to the passage vortex in the near endwall region is identified for each parameter. Ultimately, the passage vortex, displaced coolant away from the endwall at the same rate as the vorticity magnitude and size of the passage vortex is much larger than that produced from film cooling.

DEDICATION

I would like to dedicate this work to my mother and father and girlfriend for their unconditional love and support.

ACKNOWLEDGEMENTS

I would like to thank my committee chair, Dr. Schobeiri, and my committee members, Dr. Anand and Dr. Strouboulis for their guidance and support throughout the course of this research.

Thanks also go to my friends and colleagues, Ali Nikparto and Mostafa Ghoreyshi for their help and the department faculty and staff for making my time at Texas A&M University a great experience.

CONTRIBUTORS AND FUNDING SOURCES

All work for the thesis was completed by the student, under the advisement of Dr. Schobeiri of the Department of Mechanical Engineering. I would like to recognize my committee members, Dr. N.K. Anand and Dr. Theofanis Strouboulis for their guidance and support throughout the course of this research.

There are no outside funding contributions to acknowledge for this research and compilation of this document. Many of these findings and results were made possible by previous studies performed by Dr. Schobeiri's research group in the Turbomachinery Performance and Flow Laboratory at Texas A&M University.

NOMENCLATURE

BR	Blowing Ratio
C_{ax}	Axial Chord Length
CA	Compound Angle
CFD	Computational Fluid Dynamics
C_p	Coefficient of Pressure
d	Diameter
DR	Density Ratio
FCE	Film Cooling Effectiveness
h	Heat Transfer Coefficient
k	Turbulent Kinetic Energy
k_f	Thermal Conductivity of Fluid
L	Length
LE	Leading Edge
Nu	Nusselt Number
P	Pressure
PS	Pressure Side or Pressure Surface
RANS	Reynolds Averaged Navier Stokes
Re	Reynolds Number based on Axial Chord Length and Freestream Velocity
SS	Suction Side or Suction Surface
S/S_o	Normalized Surface Coordinate Distance From Leading Edge

T	Temperature
TE	Trailing Edge
Tu	Turbulent Intensity
t	Time
u or V	Velocity
W	Width
y^+	y plus
α	Compound Angle in Degrees
η	Adiabatic Film Cooling Effectiveness
ν	Kinematic Eddy Viscosity
ζ	Secondary Losses
ρ	Density
ω	Specific Dissipation Rate or Vorticity

Subscripts

aw	Adiabatic Wall
c	Coolant Fluid
exit	Geometry Exit
in	Geometry Inlet
m	Mainstream Fluid
s	static
tot	Total
τ	Turbulent

TABLE OF CONTENTS

Page

LIST OF FIGURES

Page

LIST OF TABLES

Page

CHAPTER I

INTRODUCTION AND LITERATURE REVIEW

Introduction to Subject

Overview of Gas Turbines

Gas Turbines are engines in which energy from air as a working medium is converted into mechanical energy and vice versa. These engines have been in use for over a century, and have practical applications in many different industries. There are two main categories of gas turbines: Those that are land based, mainly used for power generation applications, and those for aviation, such as commercial and military plane engines. The gas turbines used in power generation can output close to 1300 MW of energy, enough to provide electrical power to over 50,000 homes. [1] Although these large turbomachines can produce vast amounts of energy, the thermal efficiencies of these systems only reach approximately 40%. With so much energy dissipated throughout the machine, this pitfall leading to researchers' interests in improving the efficiencies of these machines. By understanding where losses occur in the machine, optimizations and new methods can be introduce to increase amount of potential power the gas turbines can produce.

Gas turbines, work in a three step thermodynamic process known as the Brayton Cycle. In this cycle, work is inputted into the system through the compressor component, which in turn increases the temperature and pressure of the working fluid. This compression process occurs over a set of blades that turn on a shaft, which increases the

pressure gradually over each stator-rotor stage. The pressure ratio seen during this compression process reaches values of 30:1. This will bring the Compressor Discharge Temperature to values around 500 °C. After this work input process, the working fluid will leave the compressor and enter the combustion chamber, where heat is added to the system. The high-pressure working fluid undergoes a combustion process with an external combustion gas increasing temperature to even higher values near 1500 °C. The last step of the Brayton Cycle will then remove the energy from the working fluid in the turbine component. Fluid will enter this portion of the machine and the high-pressure, high-energy fluid will convert energy into the rotating mechanical energy along the turbine shaft. This energy can then be stored in an electric generator, which is done abundantly in land-based applications, as seen in Figure 1.

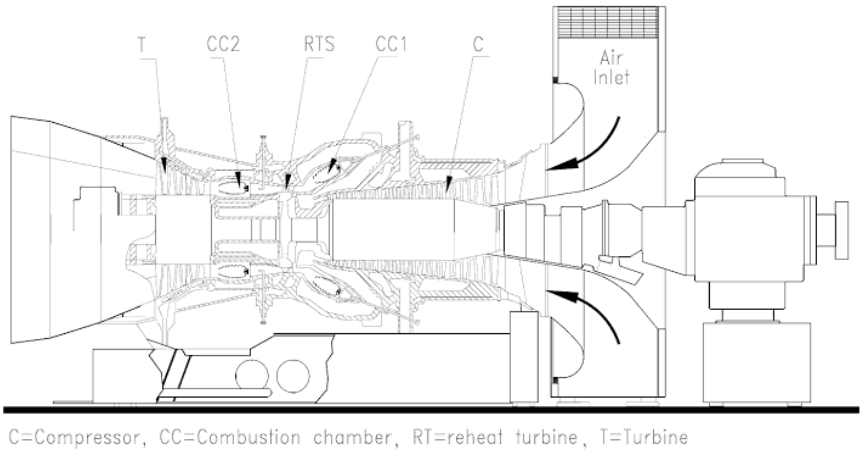

Figure 1: Cross-section schematic of GT-24 gas turbine highlighting the compressor stages, combustion chambers, and turbine stages. Reprinted from [2]

In order to increase the amount of extracted energy from the gas turbine, a higher temperature to exists entering the turbine component. While increasing the working fluid temperature is easily obtainable in the combustion process, engineering problems come into play as the working fluid enters the first few stages of the turbine. This is due to the metal temperature not being able to handle the larger thermal stresses without catastrophic failure. Researchers have been working on determining where the highest heat transfer fluxes occur on the blade surface and from there investigating methods to reduce the thermal loads on the turbine blades.

Introduction of Numerical Analysis

There are two different approaches that researchers use when investigating heat transfer applications in turbomachinery, experimental methods and numerical analysis. Experimental methods use a physical laboratory to replicate engine flow and collect data and properties of the flow through instruments and sensor. While this process of understanding is incredibly useful, it can be very timely and economically inefficient. Numerical Analysis on the other hand can be relatively quick and inexpensive to understand the flow of the fluid. By using fundamental equations and algorithms, numerical approximations on flow properties can lead to very accurate and good assumptions of how the flow can behave in many applications.

The use of Numerical Analysis in Fluid Mechanic applications is a field known as Computational Fluid Dynamics (CFD). By using high-speed supercomputers, solutions can be attained by performing calculations required to simulate fluid flow in

various scenarios. CFD is a powerful tool when used appropriately, which results can be obtained that are either impractical to reach from experiments or needed in a more timely manner.

All CFD problems are solved using the Navier Stokes equations in which the calculations are performed using finite differences methods and the geometry volume under consideration is divided into multiple small finite geometry cells. Once this geometry is discretized, physical models and boundary conditions are defined in a manner parallels the physical scenario as best as possible. Computational softwares have been developed to deliver accurate solutions quickly and robustly across a large range of applications. A particular software, which is used in this investigation, ANSYS CFX, is recognized for its applicability for rotating machinery applications in CFD.

One issue with CFD is the modeling of turbulence, the unsteady variation within fluid flow. As most engineering applications involve flow that has some level of turbulence, being able to model this turbulence as been a key subject in CFD. There are various classifications of models in which different eddy scales are considered for the fluid domain calculations.

The three universal classes are the Direction Numerical Simulations (DNS), Large Eddy Simulations (LES) and Reynolds Averaged Navier-Stokes Equations (RANS), all of which resolve or model the eddy scales in different ways. The DNS method solves the Navier-Stokes equations without any turbulence model thus considering the whole range of spatial and temporal scales of turbulence when resolving. Because of this, the DNS requires an incredibly fine mesh and is too computationally

expensive for most engineering applications. The LES method, hinting the name focuses only on the large scale eddies that are in the system. Although the computational cost is much less than that of the DNS method, the LES method has poor resolution in areas of complex geometry or flow configurations. This is where the RANS model serves as a good agreement. As suggested, the RANS model takes a time average of the values in the Navier Stokes equations Theses averages and approximations of turbulence are based on the properties of the flow and the geometries of which the flow acts upon.

While numerical analysis is a very powerful tool in Fluid Dynamic applications it is very useful in studying new methods and processes that can be used in turbomachinery applications. CFD can be utilized for optimizing blade designs for the aerodynamics in order to convert the most energy into the system as possible and also to understand where aerodynamic and heat transfer losses occur in particular blades and stages without have to fabricate and design full experimental systems. This Numerical Analysis method will be used to understand the heat transfer and film cooling across a turbine blade with complex flow considerations.

Importance of Subject

Heat Transfer in Turbine Blades

As discussed earlier, the inlet temperature on turbine blades can be very high as a result from the combustion process. The higher the working air inlet temperature is, the more work can be converted into mechanical energy in the turbine process. However, issues can arise when the working air temperature is too high. The steel used for turbine

blades have a melting point near 1400 K, therefore when the working air from the combustion process enters the turbine at temperatures near 2500 K failures will begin to occur. In order to protect the blade from high thermal stress but also to gain the most energy from the turbine process cooling schemes have been introduced in the past several decades. As seen in Figure 2 many different blade cooling schemes have been studied over the years allowing for turbine entry temperatures to increase over time.

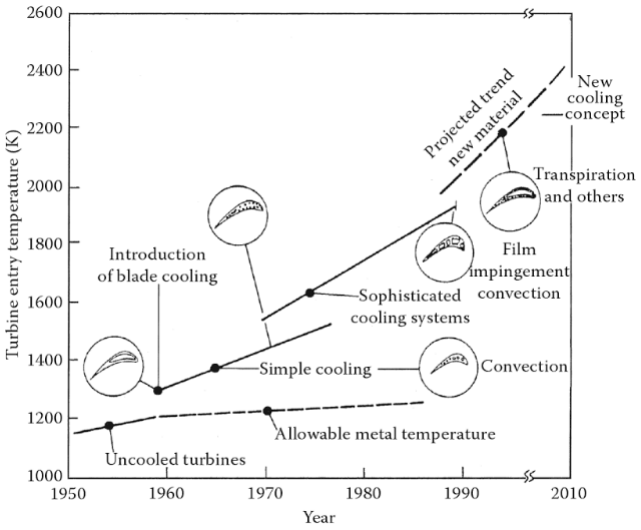

Figure 2: Variation of turbine entry temperature over recent years with the introduction of cooling schemes. Reprinted from [3]

One of the earliest methods, introduced in the 1960s is simple cooling and convection cooling of the turbine blade. This method uses cooling passages on the interior of the blade to drive heat through the turbine blade and out of the system through the high velocity coolant. In this method, the working fluid and the coolant do not have

any interaction thus providing a physical limit of how much heat can be removed before mechanical properties of the blade wall become a factor.

Another method of protecting the turbine blade from thermal loads is to use a Thermal Barrier Coating (TBC) across the blade surface. This coating is a thin layer of ceramic material that is a high insulator holding heat in the ceramic and not allowing that heat from moving into the metal turbine blade. This process will allow the working fluid to reach higher temperature but again the mechanical properties of the ceramic will be a constraint on how thick the coating can be.

Film cooling, the method of focus on this investigation, uses a secondary fluid to act as a film barrier between the working fluid and the turbine blade. This process will be discussed later in this paper. Through any cooling method, it is first necessary to know where the highest heat transfer occurs on the blade surface. The leading edge of the blade is the area most susceptible, as the kinetic energy from the hot working fluid will be converted into thermal energy when the flow stagnates on the leading edge. After this high heat transfer leading edge, the heat transfer will be lower until laminar to turbulent transition occurs or until flow separation occurs. The turbulent to laminar transition will occur early on the pressure side of the blade just past the leading edge and will occur near the trailing edge on the suction surface. The separation of flow can occur near the trailing edge of the turbine blade too, both of which will increase the heat transfer.

In addition to these two-dimensional flow effects, heat transfer will also increase near the endwalls as secondary vortices and three-dimensional flows occur in the region.

These secondary flows are known as horseshoe vortices and passage vortices. Developing from the leading edge of the turbine blade, these vortices have a large effect on the heat transfer near the trailing edge as the three-dimensional flow forces of the working fluid are increased in this region.

This three-dimensional heat transfer along this blade will be analyzed in this study and by identifying the highest heat transfer regions the blade cooling methods, specifically film cooling, can then be introduced to lower this heat transfer and allow the blade to operate in high turbine blade entry temperature conditions.

Introduction of Film Cooling

One of the schemes for cooling a turbine blade and alleviating the blade of some of the thermal stresses is a method known as film cooling. Film Cooling is performed by injecting a second low-temperature fluid from the blade wall surface to provide an insulated protective layer from the high temperature working fluid, Figure 3.

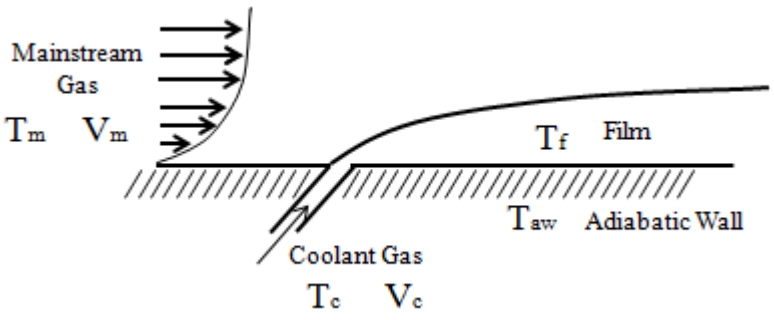

Figure 3: schematic of film cooling over flat surface with important flow parameters

The low-temperature cooling fluid (presented as coolant from this point on) is normally drawn from earlier stages in the gas turbine from the compressor component. This coolant will then have a much lower temperature than the mainstream working fluid flow, [4]. While the temperature of coolant may vary based on the application and necessary temperature that the turbine blade needs to be cooled a normalized effectiveness of the coolant on the blade surface is known as the film cooling effectiveness.

$$\eta = \frac{T_m - T_{aw}}{T_m - T_c} \quad (1)$$

This local film cooling effectiveness ranges from values of zero to one. When the effectiveness is a value of zero, the coolant does not have any effect on this region. On the other side of the spectrum, if the effectiveness is 1 this means that the region is being fully covered and protected by the coolant.

When the coolant in introduced into the mainstream from discrete holes vortices form due to the interaction of two fluids traveling initially in different directions. This three dimensional interaction, explained in detail by Fric and Roshko [5] creates four types of vortical structures, horseshoe vortices, wake vortices, jet shear-layer vortices, and most importantly a Counterrotating Vortex Pair (CRVP). The initial impulse of the coolant jets in a flow direction disturbing the mainstream flow creates this Counterrotating Vortex Pair. The impulse of the coolant interactions creates this vortex as a result of a high velocity gradient of the coolant, when this happens the coolant is entrained, or trapped, inside the CVRP disallowing for the coolant to spread. As the vortices weaken the temperature, entrainment from the coolant injection will then spread

laterally downstream. The strength and size of this vortex pair is dependent on multiple factors, those being the coolant injection inclination angle, the shape of the hole that the coolant is injection from and the momentum that the coolant has prior to injection.

This temperature relationship between the two fluids can be approximated using the ideal gas law. When the temperature of the working air increases, the density will then decrease proportionally. This ratio of density of the coolant to the density of the mainstream fluid is known as the Density Ratio (DR).

$$DR = \frac{\rho_c}{\rho_m} \tag{2}$$

While this Density Ratio can help predict the film cooling effectiveness across the blade surface, these trends seen by Pedersen, et al. [6] found that Density Ratios below 1.0 show a decrease in effectiveness as the velocity of the coolant increases. In this study, it was observed that higher density coolant stayed closer to the adiabatic surface in comparison to lower density coolants at the same Blowing Ratio, defined below. This is because the jet momentum is higher with the lower density coolants thus causing the cooling jets to lift off and not reattach and affect the surface as much.

Just as the Density Ratio is a prominent parameter used to understand the interaction of coolant fluid and mainstream fluid, another parameter that is used to quantify the fluid interactions is the Blowing Ratio. This parameter can be defined as the mass flux ratio between the coolant flow and the mainstream flow. The mass flux being quantified as the density and velocity of a specific fluid. While knowing the mainstream flow temperature and speed, and applying a Density Ratio, a known velocity of the fluid can then be obtained through the desired Blowing Ratio needed in the study.

$$BR = \frac{\rho_c V_c}{\rho_m V_m} \quad (3)$$

In experimental studies from Goldstein et al. [7], the effects of film cooling effectiveness is comparison to the Blowing Ratio. Trends were seen in which the effectiveness increased as the Blowing Ratio increased for values below 0.5. For values of 0.5 to 0.74, the effectiveness levels and for values of Blowing Ratio above 0.74 the effectiveness decreased due to jet lift off and the coolant have little to know interaction with the blade surface. Vinton et al. [8], performed a parametric study on the film cooling effectiveness on a flat plate in which both the Blowing Ratio and Density Ratio are varied, similar to this study. Through experimentation, it was found that with an increase in Density Ratio at a constant Blowing Ratio increases the lateral spread of the coolant to provide more coverage near the holes.

Leylek, et al. [9] performed a large scale computational analysis to compare numerical results to experimental results in order to understand coolant and mainstream flow interaction in discrete-jet film cooling applications. The research group found that the film coolant and mainstream flow interaction is dominated by strong three-way coupling and the flow within the film-hole was highly complex, highly elliptic in nature. They also found that the main source of turbulence moved from the shear layer above the coolant jet to the region between vortices and jetting depending on the blowing ratio, and that the blowing ratio has a large impact on the CRVP size. Ligrani, et al. [10] performed a similar study in 1994 however they investigated the CRVP with compound angle injection on a flat plate.

Just as the coolant injection rate is a large factor for cooling effectiveness, the effects of the endwall contours and secondary flow must be understood in order to cool the blade in an optimal manner. Chowdhury [11], found through experimental investigations that low turbulence loss contours exhibited a significant secondary loss core. Goldstein, et al. [12] studied the turbulent transport on the endwall between turbine blades and found that secondary flow between the turbine blades has an overall effect of increasing the convection on the endwall but the film cooling interaction between the coolant and the blade surface is reduced. Lynch, et al. [13] used RANS models to measure film cooling on contoured endwalls and found that the application of cooling was shown to reduce the spreading of coolant across the endwall due to the reduction in cross-passage flow. Additionally, the simulations over predicted the laterally averaged effectiveness because of the under prediction of the secondary flow in the CFD models.

A study from Sen [14] found that the compound angle interaction between the mainstream and coolants jets results in higher heat transfer rates with a higher momentum ratio, or rather when the Density Ratio or momentum ratio increase. A similar study on the effects of compound angle injection has been performed by Martinez [15] in which a numerical investigation was performed on a film cooled flat plat in which cylindrical holes with high compound angles injected coolant in the system. This study found that a Shear Stress Transport turbulence model best represented an experimental benchmark with the same set up configuration. While this study highlights that the effects of varying the Blowing Ratio in the system is does not

investigate the effects of endwall forces or curvature effects that exists on a low pressure turbine blade.

Curvature Effects on Discrete-Hole Film Cooling by using numerical methods were studied by Berhe and co-workers [16]. In this study, they found that for low Blowing Ratios, the convex surface (suction surface) the effect of stream curvature results in a higher cooling effectiveness. The authors also found that the concave, or pressure, surface the flow involved a stronger vorticity and greater mixing of the coolant jet with the mainstream gases. While on the convex surface, counter rotating vortices were suppressed and the coolant jet pressed to the surface by a strong cross-stream pressure gradient.

The conjunction of film coolant with flow fields near the endwall have been a focus to many authors. The effect of endwall forces have significant effects on the suction surface of the blade so that coolant does not have any influence of the blade surface in this region [17]. While the study previously mentioned Mhetras was solely an experimental investigation, a numerical analysis performance by Ling, et al. [18] focuses on the variance of compound angles on film cooled stator blades. This study shows that there is better effectiveness on the suction surface with improving blowing rate but the effectiveness decreases with a lower compound angle.

Review of Relevant Literature

Applying Numerical Analysis to applications for Turbomachinery has been a very useful tool in academia and industry. Turbomachinery flows and film cooling

applications consist of complex 3D flows with details that are hard to capture through CFD methodology. However, through mesh sizing methods and turbulence and transition models the true flow physics that occur in film cooling applications can be closely modeled.

One main concern is that most CFD models fail to capture the eddy-viscosity turbulence in the flow. In 1994, Menter [19], introduced a Shear Stress Transport (SST) two equation turbulence model. This derivation of the SST model came from a combination of the k-ε and k-ω model, both, which predict flow behavior well in free-stream and near endwall regions, respectively. More details of the equations and derivation of this model will be explained in later chapters. In 2009, Menter [20],addressed issues of 2D and 3D separation predictions, curvature effects, and turbulent transition. In this paper, he offers options and improvements to model turbulent transitions and enhancement for streamline curvature through additional equations to be implemented into the curvature model. The additions relevant to this study will be highlighted in the methodology.

Menter also recommends certain curvature correction models from Spalart and Shur [21] to accommodate the high curvature of the blade and the laminar to turbulent transition [19] that will occur in such a highly loaded low pressure turbine blade.

In a study from Auf dem Kampe, et al. [22] CFD models for a flat plate show very good agreement for film cooling effectiveness to experimental data with coolant holes having cylindrical profiles. However, for diffused holes there are over predictions for the film cooling effectiveness in low Blowing Ratio cases. They contribute this

discrepancy in the diffused hole cases to a lack of lateral turbulent diffusion in the numerical model. The high three-dimensional flow expected in this study inhibits multiple complex phenomena thus making the physics increasingly difficult to model. Lakehal [23] states that the turbulence anisotropy around the coolant injection grows more in this high complexity flow region. This turbulence anisotropy as led to authors, Bergeles [24], and to model the promotion of turbulent cross fluxes in attempt to model the coolant-air mixture accurately. Although the study by Lakehal is on a symmetric blade, the models for turbulent diffusion and lateral spreading can be applied to cases with high curvature and pressure gradients as seen for Medic, et al. [25]. While this investigation used the v^2-f turbulence model, it states empirical equations for the turbulent time scale that can predict stronger lateral spreading that other models are capable of predicting.

Germain and Baier [26] performed numerical simulations on turbine blade channels to identify the flow structure and quantity the secondary flows that are essential for the investigation of losses in a turbine blade channel. They made points on the vortex strength of the passage vortex as well the kinetic energy that the passage vortex gains as it travels across the blade channel. Alameldin, et al. [27], performed a CFD Analysis to study the increase in total losses of a transonic turbine blade subjected to film cooling.

In 2007 Laskowski, et al. [28] generated 3-D cooled flow around a high pressure turbine blade and made predictions on the conjugate heat transfer assessment on the vane geometry. This study, using the shear stress transport turbulence model and an unstructured grid, found that the CFD models slightly under predicted the heat transfer

coefficient on the pressure and suction surface. This in turn over predicts the adiabatic film cooling effectiveness in comparison to experimental data [29].

Specific Scope of Study

In this study, film cooling effectiveness near the endwall is investigated on a Low Pressure Turbine Blade. Although Low Pressure Turbine Blades do not currently exhibit film high thermal stress, many researchers expect this to be a concern in the future of turbomachinery [3]. The reason for using a Highly Loaded Low Pressure Turbine Blade is because this type of blade exhibits strong adverse pressure gradients, transitional flow, and separation bubbles. These aerodynamic phenomenon have motivating effects on film cooling effectiveness and mainstream-coolant fluid interaction.

A parametric numerical analysis is to be performed to understand the film cooling effectiveness in conjunction with the endwall in regards to heat transfer and aerodynamic properties of the turbine blade. This numerical analysis is a branch of fluid mechanics known as Computational Fluid Dynamics (CFD). Through this method of problem solving, accurate studies can be performed to understand the flow physics in the turbine blade. By varying parameters for the coolant injection angle, coolant-to-air Density Ratio (DR) and coolant-to-air mass flux ratio, many data sets can be compared and analyzed to understand how these parameters affect the film cooling effectiveness, heat transfer and aerodynamics properties of the turbine blade under specific conditions.

These CFD analysis results can then be compared to future experimental investigations for further validity. As film cooling methods have not been studied heavily and implemented for low pressure turbine blades, there is motivation to understand how film cooling schemes are effected and can be controlled through high pressure gradients and separation bubbles that occur in the downstream direction of the blade. Likewise, it is important to learn to model this physics accurately as more rigorous design optimizations can be explored in the upcoming years.

CHAPTER II

OBJECTIVE

This study focuses on the effectiveness of film cooling effectiveness on a highly loaded turbine blade in conjunction with the effects of endwall vortices. By performing numerical analysis using the commercial software CFX 17.1 the film cooling effectiveness is measured on the pressure and suction surface of a turbine blade with 6 rows for coolant injection on the pressure and suction side and a row on the leading edge. The blade rows are consisted of 27 holes near the lateral centerline of the blade that inject coolant parallel to the mainstream flow direction. The rest of the holes are angled towards the endwall, known as the compound angle, to counteract the secondary and endwall forces on the mainstream flow. By varying coolant injection direction, coolant injection temperature, and coolant injection speed, the film cooling effectiveness across the blade can be optimized to prevent thermal stresses across the blade surface. Through varying the parameters of compound angles by ±20%, Density Ratio to 0.75, 1.0, 1.2, 1.5, 2.0, and Blowing Ratios to 0.75, 1.0, 1.25, 1.5, the aerodynamics, heat transfer and film cooling vortex development near the endwall will be studied through computational fluid dynamics. By understanding the interaction between the film cooling vortices and the endwall vortices in regards to the varying parameters, a better knowledge will come for designing film cooling in this high secondary flow region.

CHAPTER III

METHODOLOGY

Physical Blade Geometry

For this investigation a "Pak B" airfoil, designed by Pratt and Whitney is used. This airfoil has a blade chord of 203.44 mm and an axial chord length of 182.85 mm. The height of the blade, otherwise known as the lateral width of the blade is 200 mm and this blade is two dimensionally symmetric. More data on the blade geometry is seen in Table 1.

Table 1: Physical blade geometry parameters

Parameters	Values
Nozzle Width	W = 200.0 mm
Blade Chord	C = 203.44 mm
Blade Axial Chord	C_{ax} = 182.85 mm
Blade Suction Surface Length	L_{ss} = 270.32 mm
Blade Pressure Surface Length	L_{PS} = 231.62 mm
Blade Height	h_{B} = 200 mm

This airfoil geometry also consists of 605 blade surface cooling holes across the blade surface. These cooling holes are distributed across 13 different rows: 6 rows on the pressure surface, 6 rows on the suction surface and 1 row on the leading edge of the blade. Each row has a twin row on the other side of the blade and they are connected to the same coolant cavity, except for the first cavity, which also includes the leading edge row, Figure 4.

Each row of consist of the 27 holes that are laterally centered on the blade with a distance of 4.2 mm between each other. These midspan holes are directed in a streamwise direction with the mainstream flow, meaning the mainstream and coolant flow are all parallel to the endwalls of the blade.

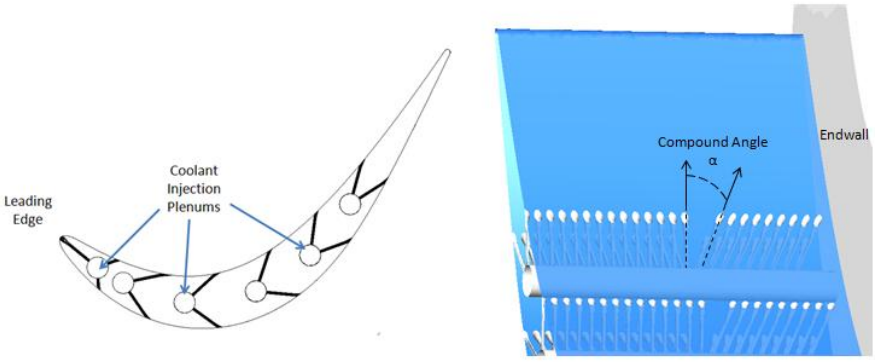

Figure 4: Schematic of profile of blade showing the 6 coolant injection plenums (left), illustration of angle definition for compound angle injection towards blade endwall (right)

In addition to the streamwise direction holes, the rest of the holes in the row are designed with a compound angle towards the wall, Figure 4. These compound angles are in place to counteract the passage vortices that are experienced near the endwall of the blade. Due to the original design and manufacturing of the blade with the compound angles, each row consist of a different number of compounded holes as well as a different injection angle and compound angle. These injection and compound angles are defined where the inclination angle is defined as how the coolant penetrates the mainstream flow relative to the blade surface, and the compound angle is defined as the

angle of which the coolant penetrates the flow in a cross-stream manner. When varying the compound angles for this numerical analysis, the inclination angles as well as the downstream position of the holes were kept constant.

Each hole also has a diffused cylindrical shape. Thus meaning the area of the hole is smaller inside the blade and as the hole gets close to the blade surface it becomes larger. The ratio between the blade coolant hole exit and inlet area is on average 3 for all holes. This ratio does vary some depending on the hole location and the blade curvature at that location. This curvature whether it is concave or convex will then make the exit area larger or smaller. Figure 5 is a schematic showing the diffused shape of all holes and the projected lateral and streamwise diameter for the hole exit on the blade surface.

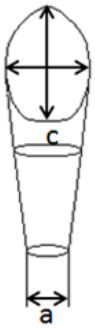

Dimension	Length
Circular Inlet Diameter (a)	1.2 mm
Lateral Diffused Diameter (b)	3.66 mm
Streamwise Diffused Diameter (c)	2.06 mm

Figure 5: Drawing showing the geometry of the diffused shape hole of blade

Ultimately, the blade geometry and dimensions of the blade will not be altered in the course of this study. The only design changes that will be made will be the alteration of the compound angle of the blade. Other physical qualities of the blade such as size

and mainstream flow over the blade will be the exact same as the experimental study that will be used as a benchmarked and will be discussed later in this chapter.

Experimental Study Benchmark

The proposed study is a numerical continuation of a study performed by Nikparto [30]. In this study, an experimental investigation was performed on a low pressure turbine blade in the cascade facility in the Turbomachinery Performance and Flow Research Laboratory (TPFL) at Texas A&M University. This facility is able to simulate the flow conditions inside gas turbine engines. The cascade facility, Figure 6, can simulate steady and unsteady inlet flow conditions by moving rods upstream of the stator blades being tested.

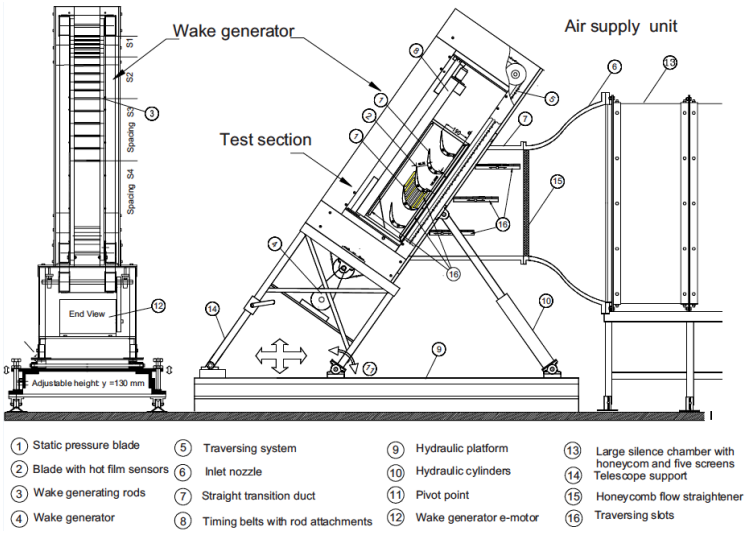

Figure 6: Turbine cascade facility at TPFL with components and adjustable test section. Reprinted from [31]

For this study a special blade, containing 605 holes distributed across 13 different rows on the blade surface, was designed and inserted into the cascade facility. The blade consisted of 6 coolant injection plenums leading to diffused rows on the blade surface. Each plenum injected a row of diffused holes on both the suction surface and pressure surface of the blade, with the exception of the first plenum having a third row of holes on the leading edge of the blade. Each row includes 27 holes that inject coolant in the streamwise direction with the mainstream fluid and between 9 and 11 holes near the endwall that inject coolant at a compound angle towards the endwall. These holes are arranged at a compound angle to contradict the effects of passage and horseshoe vortices as identified later in this paper. Data on the geometry of the blade can be seen below.

Table 2: Experimental parameters used in the experimental investigation. Reprinted from [30]

Parameters	Values
Inlet Velocity	V_{in} = 6.02 m/s
Inlet Air Angle to the Cascade	0 deg
Inlet Turbulence Intensity	Tu_{in} = 1.9%
Blade Reynolds Number	Re = 150,000
Cascade Solidity	σ = 1.248
Belt Velocity	V_B = 7.52 m/s
Blowing Ratio	BR = 1.0
Density Ratio	DR = 1.0

The experimental investigation by Nikparto studies both the heat transfer and film-cooling effectiveness of the blade. The data obtained by this study, parameters seen in Table 2 is the benchmark for the data obtained in the numerical simulations. To study the heat transfer, a liquid crystal method was used, seen in figure below, Figure 7. The blade studied in this experiment was made of a nonconductive material with a thin foil attached to its surface. Connected to this tape is a liquid crystal to record temperature measurements. By using a power system and two multimeters, the power losses can be calculated across the blade surface through voltage and currents readings across the blade terminals. This data is then reduced upon a constant heat flux analysis.

For the film cooling effectiveness measurements, the blade surfaces were covered with Pressure Sensitive Paint (PSP). The surfaces of the blade are covered with a white bases coat and 9 layers of the PSP are sprayed on top using an airbrush, applying the constant manner to ensure uniform thickness across the blade. The surfaces of the blade were then excited using a strobe light in which a corresponding color is emitted from the surface. Based on the color intensity reflected back into the camera the partial

pressure of the oxygen in the system could be measured, as pure nitrogen and air was used as the coolant. This partial pressure relationship between nitrogen and air could then be adjusted back into a concentration effectiveness analogy parallel to the film cooling effectiveness.

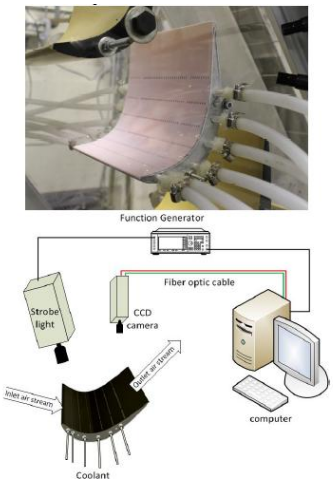

Figure 7: Instrumented blade with PSP for film-cooling effectiveness purposes (top) and data acquisition system (bottom)

This study using a Blowing Ratio of 1 with a trailing edge Reynolds number of 150,000. By using the results in Figure 8, a number of conclusions could be drawn from the experimental findings. Most of these conclusions are results that were used to be a standard and target for the CFD set up and results. First, it was seen that the Film Cooling Effectiveness on the pressure side was stronger than the suction side of the blade; this could be attributed to the difference in Blowing Ratios on the twin rows, as there is a variance in the pressure coefficients on the twin rows. Also, the convex

curvature on the suction surface acts as a agent for liftoff on the suction side holes thus producing a lower effectiveness.

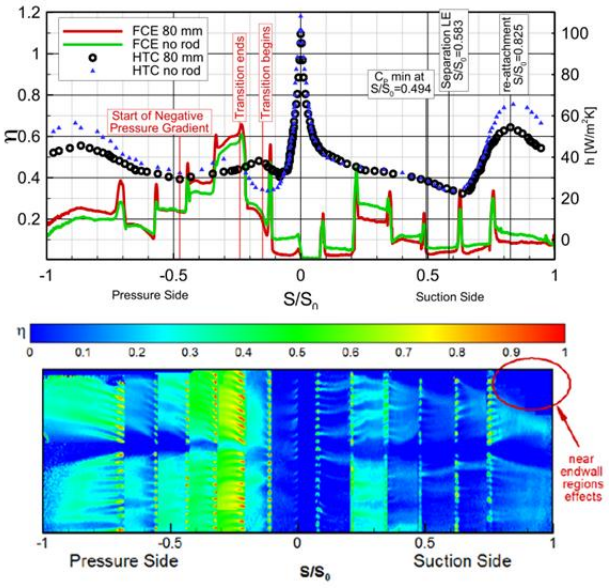

Figure 8: Experimental findings of laterally averaged film cooling effectiveness and heat transfer coefficient (top) and film cooling effectiveness contour plot (bottom) used as a benchmark with a BR = 1 and DR = 1. Reprinted from [20]

Additionally, the aerodynamics of the blade can be understood from the conclusions made in this experimental study. A separation bubble on the suction side occurs and reattaches on the trailing edge. This phenomenon can attribute to the lower FCE near the suction side trailing edge and can also attribute to the rise in the heat transfer coefficient. The passage vortices effect on the suction side can also be visualized in this experiment. From the contoured plot of the FCE the lack of distribution of the coolant near the endwall, as highlighted, is due to this passage effect. Although in this

experimental blade design, there are compound angles to counteract the passage vortices this design idea is further implemented in the numerical study by changing the compound angles.

Different Cases Studied

The parametric numerical investigation focused on the effects that the injection angle Density Ratio, and Blowing Ratio of coolant have in regards to film cooling effectiveness and heat transfer properties of the turbine blade. The Blowing Ratio is defined as the mass flux ratio between the coolant injection flow and the mainstream gas flow and the Density Ratio is the ratio of densities between the two fluids. In total, 36 different simulations were executed by varying the Compound Angle, Density Ratio, and Blowing Ratio, as seen in Table 3.

Table 3: Factor levels for all cases studied

Factor	Levels			
Coolant Injection Angle (α)	0%	-20%	20%	
Density Ratio (DR)	1.0	1.2	1.5	
Blowing Ratio (BR)	0.75	1.0	1.25	1.5

These values for the mainstream Reynolds Number at the trailing edge was selected as 150,000. This Reynolds Number of 150,000 was used in similar experimental

investigations from the research group. This reference data was used to determine accuracy in aerodynamic performance. Additionally, the Density Ratio (DR) of the coolant was investigated at values of 1.0, 1.2, 1.5, and 2.0. The Blowing Ratio (BR) was set from 0.75, 1.0, 1.25, and 1.5. This range of density and Blowing Ratios are known to produce sufficient cooling in other investigations but still do not inject enough coolant to lower the efficiency of turbine systems.

It was seen from the experimental investigation that the film cooling was ineffective at the endwall on the suction surface from $S/S_0 = 0.5$ to the trailing edge. The film cooling was also ineffective in this normalized distance on both the suction and pressure surface between the streamline and compound angle cooling holes. To vary the compound angles near the end wall of the blade the geometry files were modified using SOLIDWORKS. To modify the compound angles on the 4^{th}, 5^{th}, and 6^{th} injection row, rows in the region of poor effectiveness, the compound angles of these rows were increased and decreased by 20%. The original compound angles and new compound angles for the three rows can be seen in, Table 4.

Table 4: Compound angles in degrees of 4th, 5th, and 6th row injection holes by increasing and decreasing the compound angle by 20%

	Original Compound Angle	Compound Angle Increased 20%	Compound Angle Decreased 20%
4^{th} Row	19.70°	23.63°	15.76°
5^{th} Row	22.78°	27.34°	18.23°
6^{th} Row	25.86°	31.04°	20.69°

Governing Equations

For CFD simulations a set of mathematical equations, governing equations needed to be solved. The solving software used in this investigation was CFX. This solver uses finite element based finite volume method to satisfy the governing equations. By discretizing the domain grid, the governing equations that need to be solved for all CFD simulations are general principle equations for classic fluid dynamics: the conservation of mass equation, the conservation of momentum equation and the conservation of energy equation, altogether known as the Total Energy Equation. The equations are stated below in the Einstein Tensor format and are applicable for spatial 3-D compressible flow.

$$\frac{D\rho}{Dt} + \rho \frac{\partial u_i}{\partial x_i} = 0 \tag{4}$$

$$\rho \frac{Du_i}{Dt} = -\frac{\partial P}{\partial x_i} + \frac{\partial \tau_{ij}}{\partial x_j} + \rho F_i \tag{5}$$

$$\rho \frac{De}{Dt} = -p \frac{\partial u_i}{\partial x_i} + \phi + \frac{\partial}{\partial x_i}\left(\kappa \frac{\partial T}{\partial x_i}\right) \tag{6}$$

Where,

$$\phi = \tau_{ij} \frac{\partial u_i}{\partial x_j}$$

$$\tau_{ij} = \mu \left(\frac{\partial u_i}{\partial x_j} + \frac{\partial u_j}{\partial x_i} - \frac{2}{3} \frac{\partial u_r}{\partial x_r} \delta_{ij} \right)$$

To have fluid properties for the mainstream fluid and coolant fluid used in this equation, for density, viscosity, etc. The Ideal Gas Law was used a base assumption for these values. This Ideal Gas Law assumption is a fairly good assumption made often in turbomachinery application. This assumption relates density to the pressure and density.

$$P = \rho RT \tag{8}$$

The turbulence model used in this investigation is the Shear Stress Transport (SST) model. This two-equation model was introduced by Menter [19] inhibits the strengths of both the k-ε and k-ω, which are good in free-stream and near-wall flows, respectively. Thus, this model benefits from the k-ω model in handling the adverse pressure gradients while transitioning to handling the k-ε insensitivity to inlet turbulence properties. The two-equation model equations are given below.

$$\frac{\partial k}{\partial t} + U_j \frac{\partial k}{\partial x_j} = P_k - \beta^* k\omega + \frac{\partial}{\partial x_j}\left[(\nu + \sigma_k \nu_T)\frac{\partial k}{\partial x_j}\right] \tag{9}$$

$$\frac{\partial \omega}{\partial t} + U_j \frac{\partial \omega}{\partial x_j} = \alpha S^2 - \beta \omega^2 + \frac{\partial}{\partial x_j}\left[(\nu + \sigma_k \nu_T)\frac{\partial k}{\partial x_j}\right] + 2(1-F_1)\sigma_{\omega 2}\frac{1}{\omega}\frac{\partial k}{\partial x_i}\frac{\partial \omega}{\partial \omega_i} \tag{10}$$

In order to capture the transitional turbulence of the flow from laminar to turbulent, the correlation based transition model introduced by Menter, et al. is commonly used in commercial CFD codes. This model, known as the Gamma-Theta model, incorporates the transport equation of intermittency and couples it with the SST Turbulence Model, influencing the production term in turbulent kinetic energy downstream of the transition location. Transport equation in transitional SST model has the following form:

$$\frac{\partial(\rho k)}{\partial t} + \frac{\partial(\rho u_j k)}{\partial x_j} = \tilde{P}_k - \tilde{D}_k + \frac{\partial y}{\partial x}\left((\mu + \sigma_k \mu_t)\frac{\partial k}{\partial x_j}\right) \tag{11}$$

$$\tilde{P}_k = \gamma_{eff} P_k$$

$$\tilde{D}_k = min\big(max\big(\gamma_{eff}, 0.1\big), 1.0\big) D_k$$

The convection term is discretized using high-resolution scheme and second order backward Euler scheme for the temporal term. In solving these equations, the RMS value for the Pressure and Momentums were converged to values below 1E-6.

Boundary Conditions and Fluid Conditions

The blade simulation geometry consists of a linear cascade represented by one blade channel, presented in Figure 9. This single blade channel can be embodies a full linear cascade by applying a translational periodicity above and below the blade chord by 80 mm. The blade has wake generating rods 80 mm upstream of the blade to represent the wake of the flow caused by an upstream rotor. For this simulation, these rods stayed stationary for a simpler model. Another simplifying geometry constraint made to the blade was a lateral symmetry applied on the blade. As the full blade from experimentation was 200 mm and presented lateral symmetry, a symmetric constraint could then be applied.

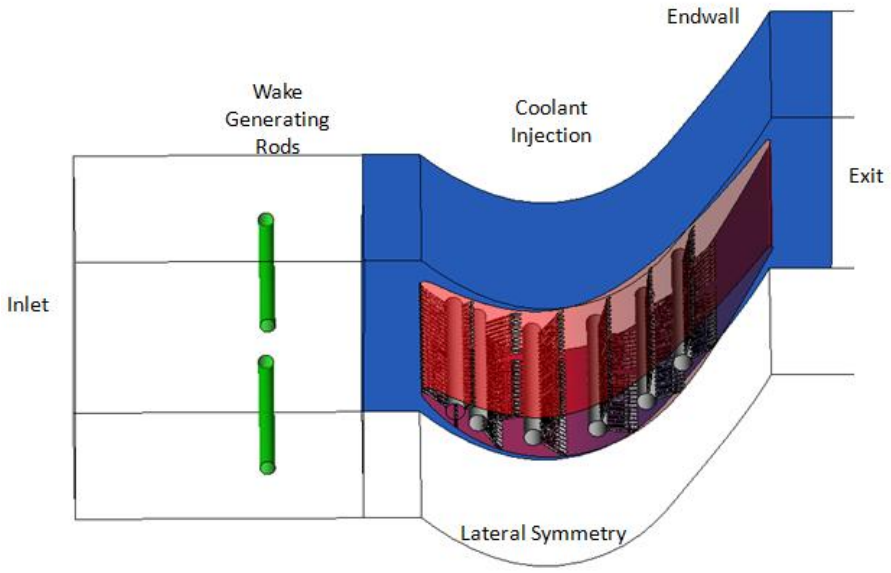

Figure 9: Geometry set-up showing boundary conditions and important features

The inlet conditions for the mainstream were based on the trailing edge Reynolds Number (Re) defined below. The inlet velocity for the mainstream flow is projected at an angle for the flow to have a zero incidence angle on the leading edge of the blade. The temperature and Turbulent Intensity set in CFX were 1500 K and 1.9%, respectfully, just as it was in the experiment.

$$Re = \frac{V_{exit} c_{ax}}{\nu} = 150{,}000 \tag{12}$$

An outlet condition for an Average Static Pressure to be 0 Pa. This outlet boundary condition is imposed as the flow downstream of the blade vents to the atmosphere, no longer interacting with the blade region. The walls of the blade as well as the endwall were represented through nonslip adiabatic walls. In the regions in which the viscous forces and fluid interactions are going to be highest, a y+ plus value is set at

unity to ensure valid results for the Turbulence Models used. These boundary conditions are show in Table 5.

Table 5: Boundary conditions for CFD geometry

Section	Boundary Conditions
Mainstream Inlet	Temperature 1500 K Velocity Trailing Edge Re 150,000 Turbulence Intensity 1.9%
Mainstream Outlet	Average Static Pressure [0 Pa]
Coolant Inlet	Mass Flow Inlet Based on Blowing Ratio Temperature Based on Density Ratio Turbulence Intensity 5%
Pressure Surface, Suction Surface, Endwall	Adiabatic, Smooth Wall, No Slip Condition
Blade Lateral Midspan	Symmetry
Blade Pitchwise Midspan	Transitional Periodic
Wake Generating Rods	Stationary Adiabatic, Smooth Wall, No Slip Condition

As the coolant mass flow rate is used as a boundary condition, this value for a flow rate varied depending on the desired Density Ratio and Blowing Ratio for each case used in the investigation. Figure 10 shows a flow chart to explain how the Density Ratio and Blowing Ratio are used to define the coolant mass flow rate. The mainstream velocity can be found by the mainstream Reynolds Number prescribed to the geometry, in this case Re = 150,000, thus giving a mainstream velocity of 6.02 m/s. The coolant temperature, and in turn density, used for these calculations was found using the ideal gas law. By multiplying, the density of the mainstream fluid by the Density Ratio, the coolant density, and coolant temperature was then determined and set as a boundary condition. Finally, by knowing the Coolant Density, the Coolant Injection Area, and the

Mainstream Density and Velocity, the mass flow rate was calculated for the desired Blowing Ratio.

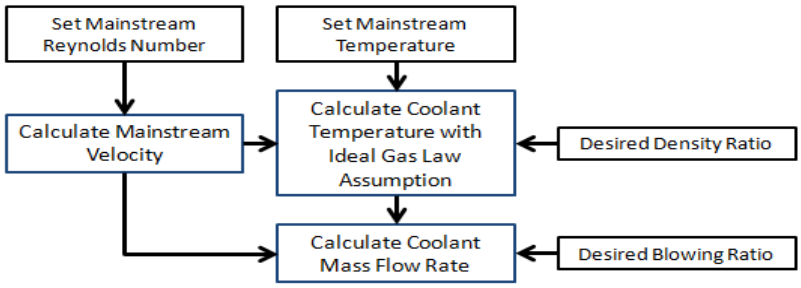

Figure 10: Flowchart of parameter dependence in CFX-Pre

Mesh Setup

To set-up the Geometry and Grid Generation the commercial software CFX Meshing v17.1 [32] was used. This software creates a hybrid-unstructured and fully tetrahedral mesh throughout the 3D geometry. For the zones of the mesh away from the blade surface and endwall, a coarse unstructured mesh was used. In the zones near the blade surface, whole cavities and endwall an inflated mesh was implemented to account for boundary layer development in these critical regions of flow. These grid implementations can be seen in Figure 11.

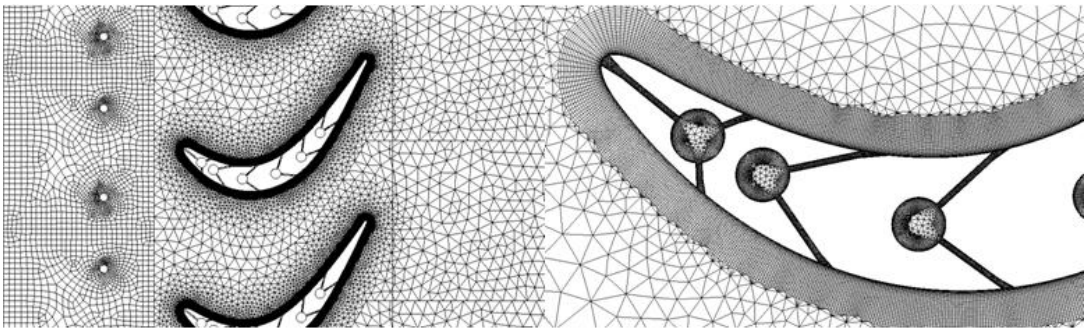

Figure 11: Mesh generation of full blade linear cascade profile with spanwise spacing of 160mm(left), boundary layer inflation generation near film cooling holes and leading edge of blade(right)

The grid generation in the high complexity regions is inflated with a y^+ value near unity. This inflation has been stated as sufficient in the CFX Solver Guide [32] as an appropriate inflation to account for the aerodynamics and heat transfer properties in this high action region. The inflated region with a starting cell height of 0.075 mm was made to have a total thickness of 20 mm. This was done to capture the full boundary layer development inside the coolant cavities, on the blade surfaces and on the endwall of the prescribed geometry, Figure 12. The equation below shows how the y+ value is used to calculate and determine the first layer cell thickness inside the boundary layer.

$$y^+ = \frac{u^* y}{\nu} \tag{13}$$

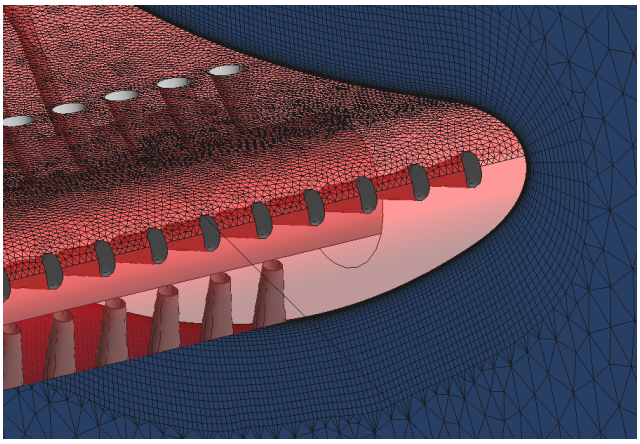

Figure 12: Inflation from blade surface (red) and endwall (blue) to capture the 3D effects from passage flow

Each injection hole had approximately 8 elements across the diameters. In total, the mesh used had 15.5 million elements. A grid independence study was conducted using the film cooling effectiveness average profile across the blade surface as a checking parameter. This is because the temperature of the blade is the most important property in this study. To confirm the grid independence a normalized average of the film cooling effectiveness was taken with coolant injected in the third and fourth row with a Blowing Ratio and Density Ratio both set at 1. The averaged value used to determine the grid independence was taken from a distance 10mm downstream in the streamwise direction from the coolant injection in the fourth row. The selected grid sizes for the study and the corresponding results are given below in Figure 13.

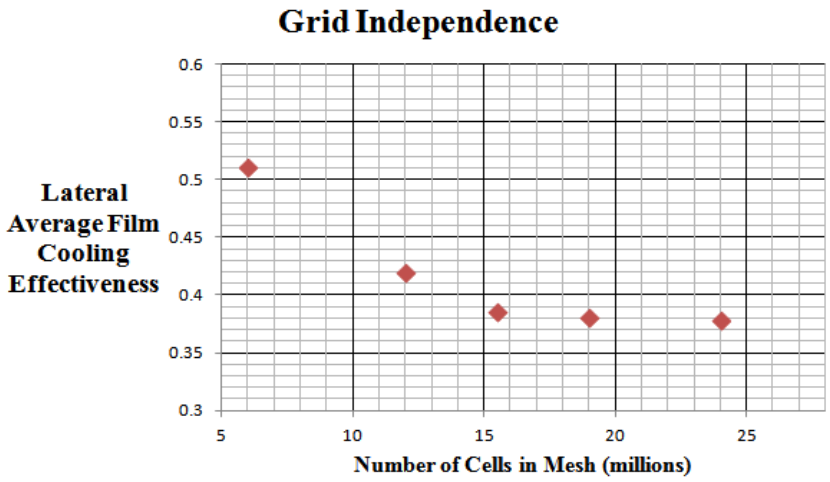

Figure 13: Grid independence study with the parameter of interest being the laterally averaged film cooling effectiveness at 10mm downstream of 4th row injection with BR = 1 and DR =1.

The grid selected was the 15.5 Million Element grid as it had a laterally average film cooling effectiveness difference of 1% with the larger meshes. In order to save computational time without losing quality in the results, this mesh size was used for all simulations. The results for these simulations are presented and discussed in the following chapters.

CFX-Solver is a finite volume method solver to solve the Total Energy Equations with the turbulence model and model modifications as described earlier. By using the Boundary Conditions as described in Table 5, the solving software achieved solutions by reaching Root Square Mean (RMS) Values targeted at 10^{-6} across all volumes. To reach this convergence a High Resolution Advection Scheme and Turbulence Numerics setting was used in order to resolve the detail of small scaled turbulence. More information on these Numerics can be found in the CFX-Solver Theory Guide [32]. When this

convergence criteria was achieved, taking a maximum of 150 iterations the solver produced results, which are to be described in the following chapter.

CHAPTER IV

DATA REDUCTION

This section gives a detailed description of how the data was processed once CFX-Solver created results. From the CFX-Solver, solutions were provided for all variables in the aforementioned Total Energy Equations. These variables were solved for every node point throughout the entire geometry. As this investigation focused on the aerodynamics, film cooling, and heat transfer on the turbine blade surface in conjunction with the endwall, variables from these specific nodes were extracted.

For aerodynamics, the velocity from the suction surface was extracted in order to see the separation and back-flow on the blade surface due to high pressure gradients. The pressure across the blade surface was also extracted to understand where separation occurred as well as the highest pressure gradients, this could help understand how the film coolant behaved in the parallel injection regions. The secondary flow effects were processed at normalized lengths across of the suction surface, by extracting vector fields and secondary losses at these locations, the compound angle and density and Blowing Ratios could be directly related.

For heat transfer and film cooling effectiveness investigations, the film cooling effectiveness values were extracted from every node on the pressure and suction surface. These node locations were there normalized relative to the distance between the leading edge and trailing edge of the respective surface. These film cooling effectiveness contours can explain the endwall effects and the spreading of coolant near the endwall

region as well as give an idea of how much the compound angle affects this effectiveness. Finally, laterally averaged values of film cooling effectiveness and heat transfer coefficient are calculated using an in-house MATLAB code to average values in the lateral direction. These averages are then shown relative to the normalized distance from the leading edge.

All data processed from the CFX-Solver were processed and normalized in MATLAB and visualized through Tecplot Software. These results from the data reduction can be visualized and further explained in the flowing chapters. All trends and conclusions stated from this investigation were drawn from these processed results.

CHAPTER V

RESULTS AND DISCUSSION

The following section will highlight the results seen by comparing the numerical investigation to the experimental benchmark, performed by Nikparto [30]. These results will include both aerodynamic parameters and heat transfer parameters that were important in the experimental investigation. By identifying the trends and magnitude of difference between the two studies the extension of results derived by varying different parameters in the numerical investigation are shown. These results will in turn study the film cooling effectiveness near the endwall and the effects of the passage vortex with the variance of the different parameters.

Experimental Benchmark Comparison

The Surface Distribution of the Static Pressure Coefficient around the blade surface is shown in Figure 14. The Pressure Coefficient, shown below, is the ratio of the static pressure difference to the inlet dynamic pressure. The experimental data used static pressure taps that were placed at the lateral midsection around the blade. The pressure taps were then connected to pneumatic pressure transducers. In the same fashion, the static pressure coefficient captured in the numerical model was also taken at the lateral midsection, or symmetric plane.

$$C_p = \frac{P_s - P_{s,in}}{P_{tot,in} - P_{s,in}} \tag{14}$$

The overall pressure coefficient distribution is accurately modeled in comparison to the experiment with the Pressure Side of the Blade having a maximum Pressure Coefficient of approximately 1.3 at $S/S_o = 0.35$ and a minimum Pressure Coefficient of -3.6 at $S/S_o = 0.5$. The solid lines in this figure show the pressure coefficients with and without coolant injection. The sudden changes on the suction side of the blade indicate the location at which coolant is injected on the blade surface. These effects due to coolant injection on the pressure surface are not as prominent due to the different in pressures of twin injection holes. This difference of pressure at each injection row results in a higher Blowing Ratio on the suction side of the blade compared to the pressure side of the blade, however the average Blowing Ratio for each row cavity was still equal to 1 for all simulations.

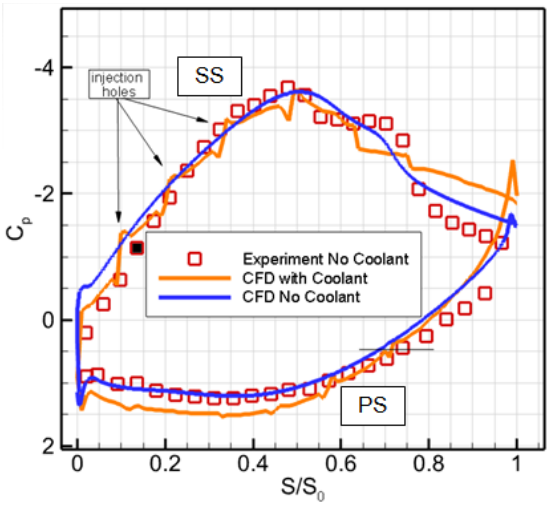

Figure 14: Pressure coefficient distribution across the blade surface for experimental benchmark without cooling and for the CFD simulations with coolant and no coolant injected

It can be seen clearly in the static pressure coefficient distribution that on the suction side of the blade near the trailing edge, there exist a separation bubble, which is apparent due to the constant pressure plateau seen between $S/S_o = 0.58$ and $S/S_o = 0.82$. This separation bubble is attributed to the high negative pressure gradient followed by the strong adverse pressure gradient on the Suction Surface, which can clearly be seen in Figure 14.

Likewise, the separation bubbles are visualized on the suction surface of the blade for the same three cases (uncooled experiment, uncooled CFD, and cooled CFD) in Figure 15. The experimentally uncooled blade shows a separation bubble extending across the region previously described above, while the CFD model for the uncooled blade predicts a separation bubble that starts slightly sooner at $S/S_o = 0.50$ and ends at $S/S_o = 0.79$. This earlier onset of separation can be explained by the coolant injection row being located just before the separation onset, even though no coolant is being injected. The CFD model with also predicts a low velocity region downstream of the last coolant jet delaying the separation reattachment in the cooled case. This coolant injection from the suction surface promotes the continued separation as the coolant interferes with reattachment of the separation bubble. This promotion of continued separation can be accounted for by the liftoff created by film cooling injection. As the blade is convex in nature on the suction side, jet lift-off is more evident in this region thus prohibiting the reattachment.

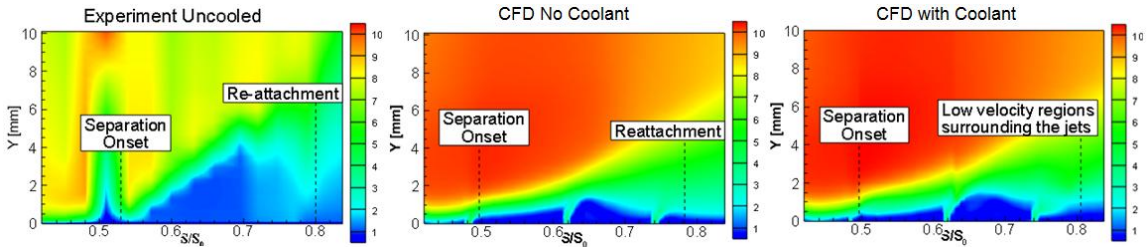

Figure 15: Separation bubble on suction side of blade for uncooled experiment (Left), uncooled CFD (center) and film cooled CFD (right)

One key difference in the experimental separation bubble and CFD RANS Model Separation Bubble is the size of the separation bubble. In the experimental case, the separation bubble size has a peak height of approximately 4 mm from the blade surface. However, in the CFD Model the separation bubbles have a maximum height of less than 2 mm. This difference in separation bubble height predicted in the numerical model is going to have significant effects on the under prediction and over prediction of heat transfer and film cooling effectiveness, respectively, later in the results. This difference in size of the separation bubble is due to the prediction of the Velocity Fluctuations in the RANS Model, Figure 16.

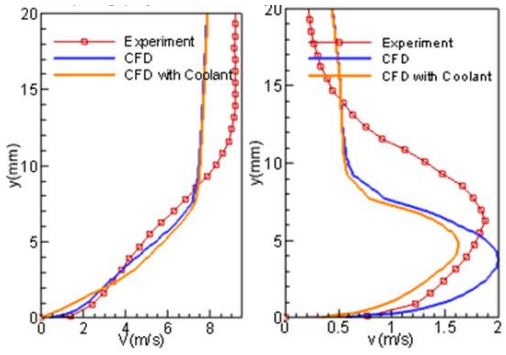

Figure 16: Velocity (left) and velocity fluctuation (right) profiles in the boundary layer for the experimentally uncooled, CFD uncooled and CFD cooled cases at S/S0 = 0.85 on the suction side

The velocity profiles along the suction side of the blade are accurately predicted in comparison with the experimental model, the solid lines representing the CFD models for the cooled in uncooled case. It should be note that the Velocity Fluctuations in this region are predicted with close magnitude, but with the fluctuations having a maximum value closer to the blade wall in the CFD Models. For this case shown (S/S_o = 0.85) on the suction surface, the maximum velocity fluctuation of 1.9 m/s occurs at a distance of 6 mm from the blade surface in the experimental model, however the maximum fluctuation of 2 m/s (uncooled) and 1.7 m/s (cooled) occur at a height of 4 mm.

These velocity fluctuations are defined by the Reynolds Stress Tensor, which is then used to predict the heat transfer in the Total Energy Equation. As these velocity fluctuation profiles are over predicted near the blade surface this is going to have an impact on the mass, momentum and energy transfer in this boundary layer region. The existence of these strong fluctuations of the velocity components near the blade surface will result in higher predicted mass, momentum, and energy transfer, thus giving an

underprediction of the heat transfer coefficient on the blade surface in the numerical models.

In comparing the heat transfer predictions of the CFD Models compared to the experimental methods, good agreement is seen in the trends of the heat transfer coefficient and film cooling effectiveness across the blade surface. In Figure 17 and Figure 18 the laterally averaged Nusselt Number and Film Cooling Effectiveness Distribution are shown across the normalized distance from the leading edge on the Pressure Side (left) and Suction Side (right) of the blade for the experiment and computational model. The Nusselt Number and Film Cooling effectiveness are defined below.

$$Nu = \frac{hc_{ax}}{k_f} \tag{15}$$

$$\eta = \frac{T_m - T_{aw}}{T_m - T_c} \tag{1}$$

The Nusselt Number, nondimensional heat transfer coefficient, Distribution shows a very high heat transfer coefficient at the leading edge of the blade for both studies. This high heat transfer is due to the large deceleration of the mainstream fluid resulting in the transfer of kinetic energy to thermal energy in this region. The development of the laminar boundary layer is characterized by the lack of lateral turbulent fluctuations not capable of mass, momentum, and energy to the blade surface results in an immediate drop in *Nu* until transition from laminar to turbulent flow develops. Additionally, the Nusselt Number Distribution Model shows a rise in heat transfer coefficient in the separation region on the suction side of the blade. Because

Separation occurs due to a strong adverse pressure gradient, high turbulent fluctuations occur in this region increasing the exchange of mass, momentum, and energy within the boundary layer resulting in a rise in *Nu*. As a whole, the *Nu* is under predicted across the entire blade surface. This underprediction of the heat transfer coefficient is due to the over prediction of the mass, momentum, and energy as explained earlier in the section. Because of the over prediction of velocity fluctuations in the boundary layer more energy is going to be predicted thus giving a higher temperature gradient and in turn a lower heat transfer coefficient. However, the overall trend in *Nu* matches the experimental distribution fairly well.

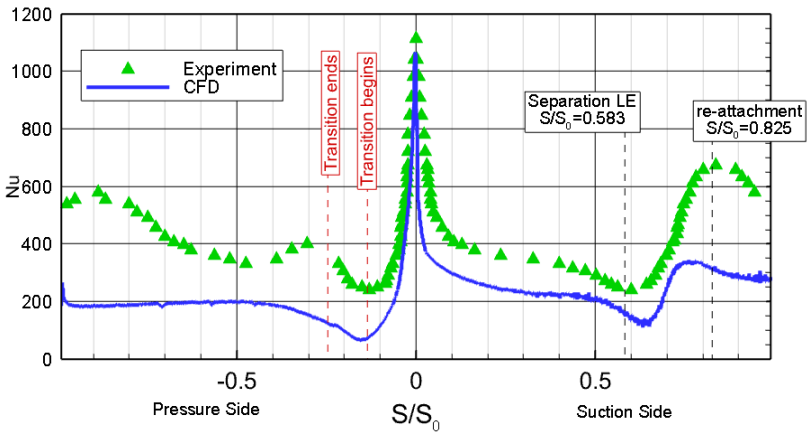

Figure 17: Laterally averaged Nusselt Number distribution on the suction surface and pressure surface for the experimental benchmark and computational simulation

Just as the *Nu* Distribution is under predicted in the numerical model, the film cooling effectiveness is constantly over predicted in the model in comparison to the experimental findings, Figure 17. Although the Blowing Ratio is held at a constant value

of 1 for both the experimental and computational model, the film coverage varies dramatically across the blade surface. In regions close the leading edge, the film cooling effectiveness is a minimum where the heat transfer coefficient is a maximum. The film cooling effectiveness is higher on the pressure side of the blade than the suction side of the blade in all regions for both the experiment and CFD model. This is because the pressure side of the blade is concave in nature allowing the film coolant to reattach to the surface while the suction side of the blade surface is convex allowing for more coolant jet lift-off and less reattachment.

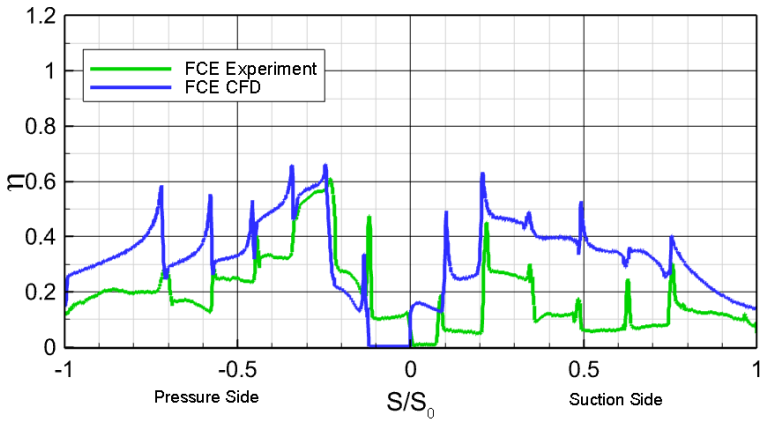

Figure 18: Laterally average film cooling effectiveness distribution on the suction side and pressure side for the experimental benchmark and computational simulation

Other important features to notice between the experimental model and computational model are that the CFD calculations constantly over predict the distance of which the film coolant fully reattaches, thus giving a slight decrease in effectiveness, the farther the location is away from the injection hole. This is due to CFD models under

predicting the turbulent lateral diffusion [22]. An isotropic turbulence model is used to calculate the lateral diffusion of the film cooling jet under predicting the decay in effectiveness of diffused holes as seen in this study. Additionally in some regions, this film cooling over prediction might reach values of 100%, mainly on the suction surface in regions of the highest convex curvature. This can then be attributed to the over prediction of the velocity fluctuations in this region resulting in a higher film coolant reattachment and less lift-off than that of the experimental case.

The film cooling effectiveness and heat transfer coefficient distributions presented thus far are blind to the three-dimensional effects that vary in the lateral direction, which is important to this study. The following discussion of figures presented considers these three-dimensional effects. Figure 19 represents the *Nu* Distribution across the blade surface in conjunction with the endwall effects. This image represents the same distribution seen in Figure 17; however, this figure now considers the development of the passage vortex on the endwall.

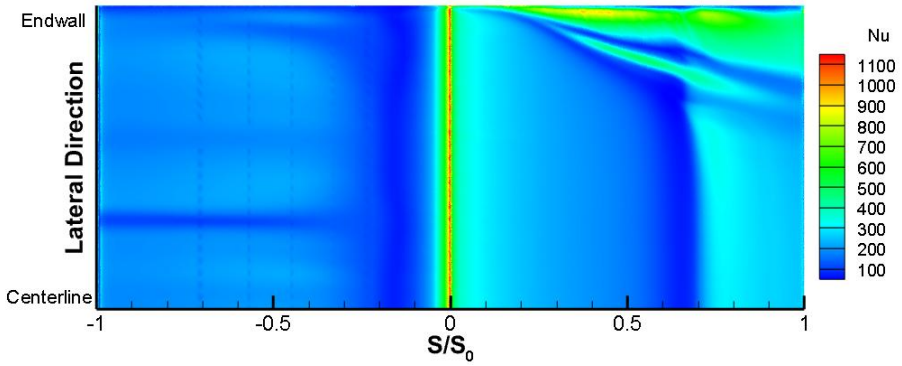

Figure 19: Contour image of Nusselt Number distribution of across the suction and pressure surface in the computational simulation

It can be seen that the heat transfer coefficient is once again highest on the leading edge of the blade and is much smaller in magnitude towards the trailing edge. The horseshoe vortices that develop due to the endwall boundary layer coming in contact with the leading can be visualized with the increase in heat transfer coefficient near the endwall of the blade. The reason for this vortex development on the suction side of the blade, as opposed to the pressure side is due to the difference in pressure of adjacent blades. The horseshoe vortex that develops on the pressure side of one blade will carry across the blade channel and come in contact with the suction side of the adjacent blade, seen in the top of the image. This passage vortex, will increase the heat transfer coefficient from the peak of curvature (S/S_o = 0.25) to the trailing edge of the blade, growing in size [12]. The magnitude of the heat transfer coefficient in this passage vortex region reaches values near 600 while in the blade Midspan the Nu values are near 200. The separation bubble heat transfer coefficient effectiveness can also be seen in this image at a suction side location of S/S_o = 0.7. to the trailing edge.

The three-dimensional film cooling distribution and effectiveness is seen in the contour images of Figure 20 comparing the experimental investigation (bottom image) to the numerical investigation (top image). The two models again show the same trends with the film cooling injection performance; however, the film cooling effectiveness magnitude is higher in the computational model as previous explained. Some important features in this image need to be discussed though. Coolant injected from the leading edge row attaches to the pressure side of the blade in the experimental model however, the coolant attaches to the suction side of the blade in the numerical model. This discrepancy can be explained due to the incorrect performance of the production limiter in the region, thus incorrectly predicting the path of the coolant being introduced into the channel. Secondary, it can be noted that the coolant injected from the discrete holes have minimal interaction between each other until far downstream from the holes. This lack of interaction between adjacent holes is correctly predicted in the computational model. Lastly, the film cooling distribution is minimal in the near endwall region on the suction side of both models. This lack of film cooling distribution in this region is attributed to the high secondary flow of the passage vortex as described and highlighted earlier. This region of high secondary flow and no coolant distribution will be a topic of interest later in this chapter.

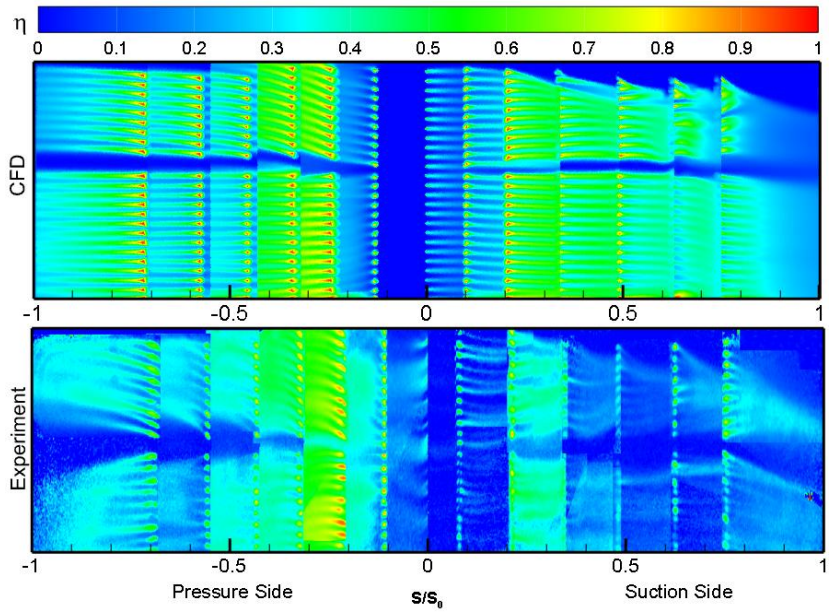

Figure 20: Contour image of film cooling effectiveness of across the suction and pressure surface in the computational simulation (top) and experimental investigation (bottom)

From comparing the Numerical Model Results with a Density Ratio and Blowing Ratio of 1 to the Experimental Benchmark from Nikparto, it can be seen that overall the aerodynamic and heat transfer trends from the CFD closely follow those of the experimental investigation. However, the numerical model under predicts the size of the separation bubble and magnitude of the heat transfer coefficient. This under prediction can be attributed the RANS Model incorrectly predicting the velocity fluctuations in the boundary layer thus predicting more mass, momentum, and energy transfer in the boundary layer in the numerical model [33]. This factor is what over predicts the film cooling effectiveness across the blade surface. However, with an accurate prediction of overall trends and passage vortex development, a continuation by varying compound

angle injection, Density Ratio, and Blowing Ratio cases are performed and discussed in the following sections.

Development of Film Cooling Vortices and Film Cooling Effectiveness

In order to understand the effects that the film cooling vortices have near the endwall in conjunction with the passage vortex effect, the film cooling vortex development away from the endwall must be understood. As discussed in earlier chapters, when coolant is introduced to the mainstream two Counterrotating Vortices (CVRP) develop due to the sudden change in velocity of coolant in the mainstream. This Counterrotating Vortex Pair will entrain the lower temperature coolant gas in between the vortices and will not allow for interaction between two adjacent injection holes.

This Vortex Pair and Thermal Interaction are shown in Figure 21 for coolant injected near the midspan of the blade on the suction side. In this region, far from the endwall region, the coolant is not affected by the secondary flows of the passage vortex. In Figure 21 the tangential velocity field normal of the blade wall (top) is displayed near two adjacent cooling holes. The corresponding vorticity contour plots are overlaid on this velocity vortex field in a manner that the red region represents the counterclockwise vortex rotation and the blue region represents the clockwise vortex rotation. In which Vorticity is defined by:

$$\vec{\omega} = \nabla \times \vec{v} \tag{16}$$

The bottom image highlights the same vorticity contour plot with the corresponding normalized temperature profile field on the same plane, displayed using lines representing the magnitude of the film cooling effectiveness.

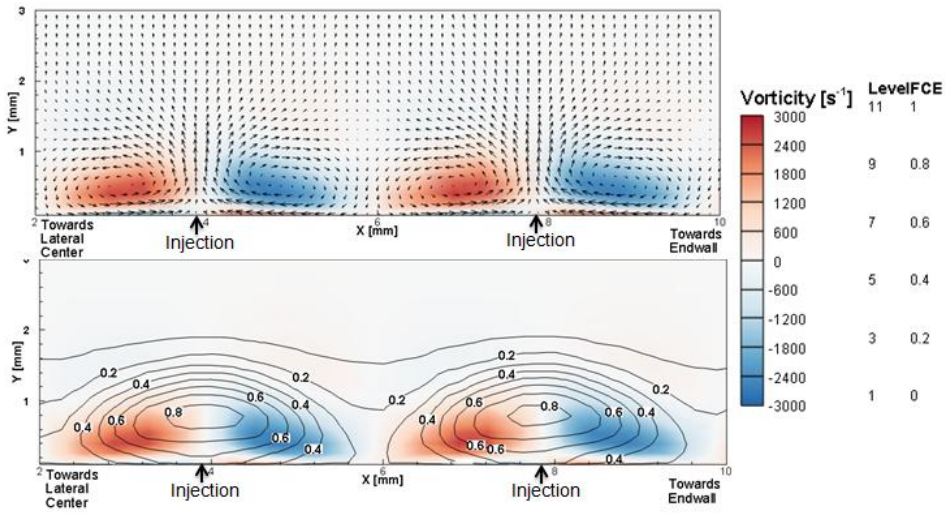

Figure 21: Film cooling counterrotating vortices highlighted through a flooded contour with the tangential velocity vector field (top) and film cooling effectiveness contour lines for no compound angle injection far from the endwall

Figure 21 is taken 2 coolant hole (5 mm) Downstream in the streamwise direction with a Density Ratio and Blowing Ratio of 1. In this case, the maximum vorticity magnitude at the center of the film cooling vortices is 2600 s^{-1}. The height of these vortex effects is 2 mm from the blade surface. It can be noted that the CVRP is completely symmetric for each film cooled hole. This symmetry is because the coolant injection only has an inclination in this image and no compound angle and no effects due to the endwall, therefore injection and vorticity is completely two-dimensional. The

interaction between two holes from a thermal point of view is also a minimum when only slightly downstream of the hole injection. The highest FCE is at a value of 0.8 as the coolant as already interacted strongly with the mainstream. This point of highest effectiveness takes place in line with the injection hole and the thermal distribution is again symmetrical between the two holes due to the symmetric nature of the CVRP. This symmetric vortex pair allows for a high coolant gas entrainment in this region and very little thermal interaction between the two adjacent coolant holes.

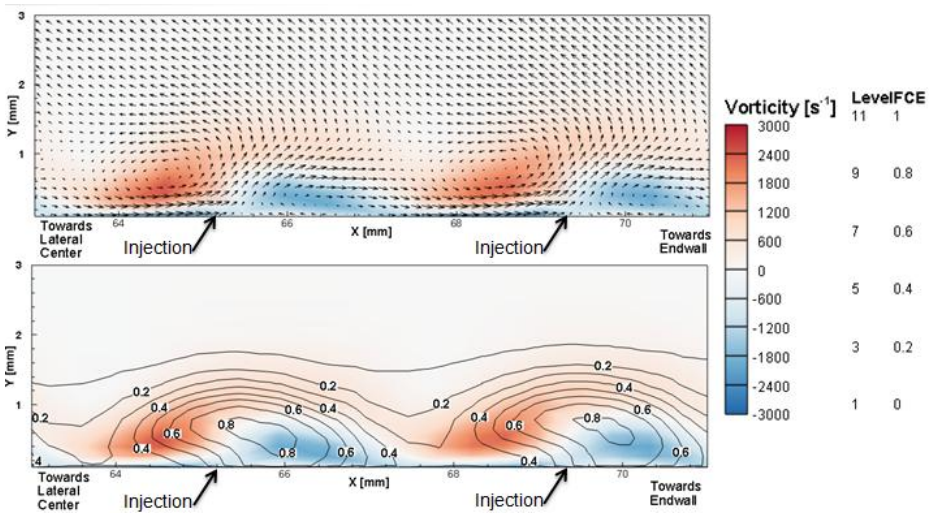

Figure 22: Film cooling counterrotating vortices highlighted through a flooded contour with the tangential velocity vector field (top) and film cooling effectiveness contour lines for compound angle injection far from the endwall

In Figure 22 there is now compound angle provided to the two adjacent cooling holes with a BR =1 and DR =1. This set up is the exact same as the previously

mentioned setup however the film coolant is injected at a compound angle of 19.70° towards the endwall.

In this figure, there are no endwall effects, as the passage vortex has no influence on this region. It can be noted that the CRVP is no longer symmetric as it was in the no compound angle injection. The overall height of the film cooling CRVP is the same however, one of the vortices is suppressed to the introduction of a compound angle. The vortex in the same direction as the compound angle is suppressed and this is due to the introduction of coolant in this direction allowing for a larger rotating vortex growth, a higher velocity gradient region on the left side of the injection hole, noted by the red vortex. Because the CVRP is no longer symmetric, the thermal distribution of the film coolant is no longer going to be symmetric. Due to one vortex being larger in size than the other is, coolant will spread laterally more that direction. These lateral spreading results in more immediate coverage of film coolant in between adjacent holes. This same effect has been seen and verified in Ref. [10].

The following sections will discuss the dissipation of strength of the CRVP as well as the film cooling entrainment and distribution. The strength and size of the CRVP is measured at 3 different locations throughout this study, highlighted in Table 6 and Figure 23. These distances are immediately from the injection location, 5 mm, or 2 injection hole diameters, downstream in the streamwise direction, and 10 mm, or 4 injection hole diameters, downstream in the streamwise direction. It was seen that farther downstream than 10 mm away from the injection hole the CRVP lost its vorticity and the film coolant for two adjacent rows was intermixed.

Table 6: Normal plane distance that film cooling injection row that the vortex and passage vortex were captured

Region	Location
A	At Injection Hole
B	2 Injection Hole Diameters away in the streamwise
C	4 Injection Hole Diameters away in the streamwise

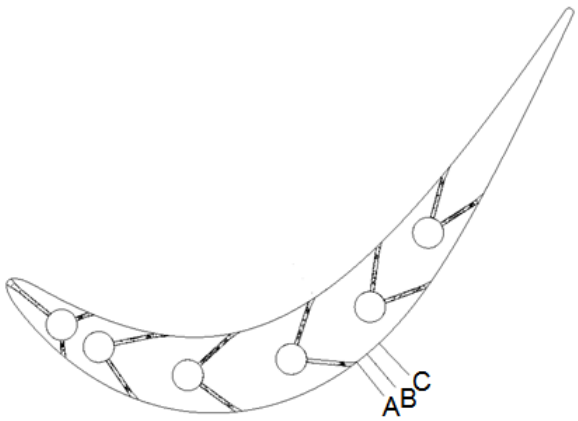

Figure 23: Schematic showing the plane at which the film cooling vortices and passage vortex were captured

The vorticity of the CRVP losses strength quickly downstream from the injection location as seen in Figure 24, where the descending rows show locations A, B, and C, respectively. While these film cooling vortices show injection with and without a compound angle without any endwall effects it can be seen that the vorticity drops from 5000 s^{-1} from the injection location to 200 s^{-1} just 4 injection diameters downstream in the streamwise direction. This large drop in vorticity strength by an order of magnitude results in more interaction between adjacent hole coolant paths. The coolant gas is no

longer entrained in the high film cooling hole vortex and thermal interaction begins to take place between the rows.

The key difference in the injection angles without endwall effects is the size and shape of the CRVP. With a compound angle injection, the CVRP is asymmetric as discussed earlier but the strength of the vorticity is of the same magnitude at parallel downstream locations. Also, the lateral spreading of film coolant is more apparent with the compound angle injection but adjacent hole interaction is very similar.

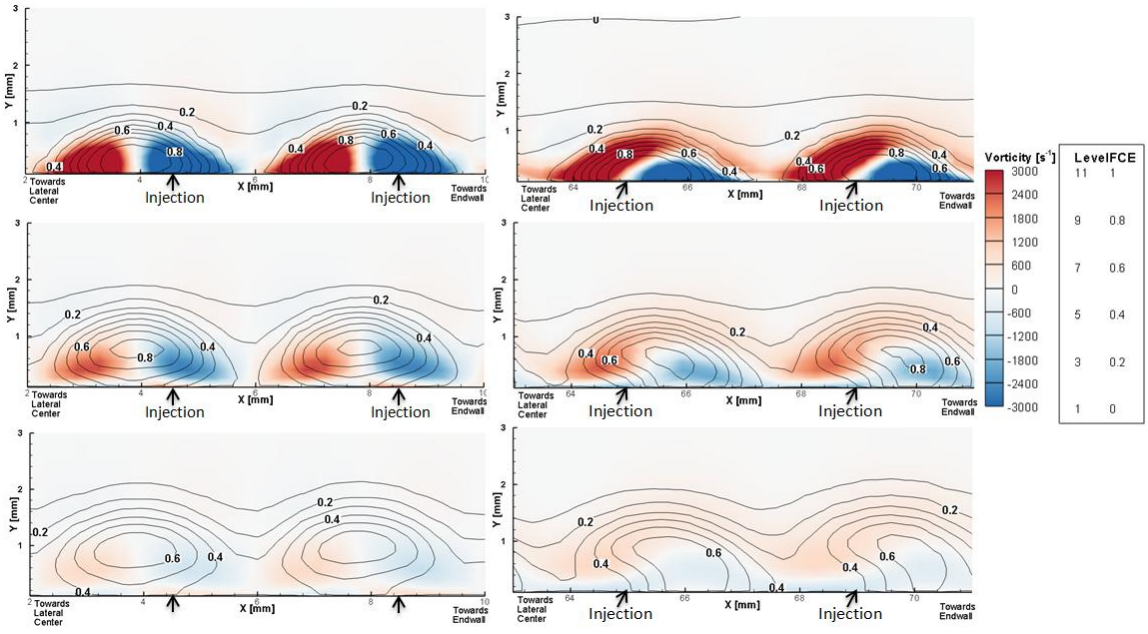

Figure 24: Development of the film cooling vortices and film cooling effectiveness distribution downstream from the injection hole for no compound angle (left column) and compound angle injection (right) without an endwall effects for BR =1 and DR =1.

While the strength of the CRVP significantly decreases only 10 mm downstream of the injection location this will have significant impacts on how the film cooling performance is on the Passage Vortex Region. The passage vortex is much larger in size and also does not lose strength but gain strength as it travels across the blade channel. The passage vortex, in this case, has a vorticity magnitude of 10,000 s^{-1} which is much larger than the vorticity of the film coolant vortices at the injection location. The larger vorticity of the passage vortex is immediately going to displace the film coolant as seen in Figure 25. In this figure, the right side of the image represents the endwall at location of 100 mm away from the lateral center. The closest film cooling injection hole to the endwall is 7 mm away from the endwall.

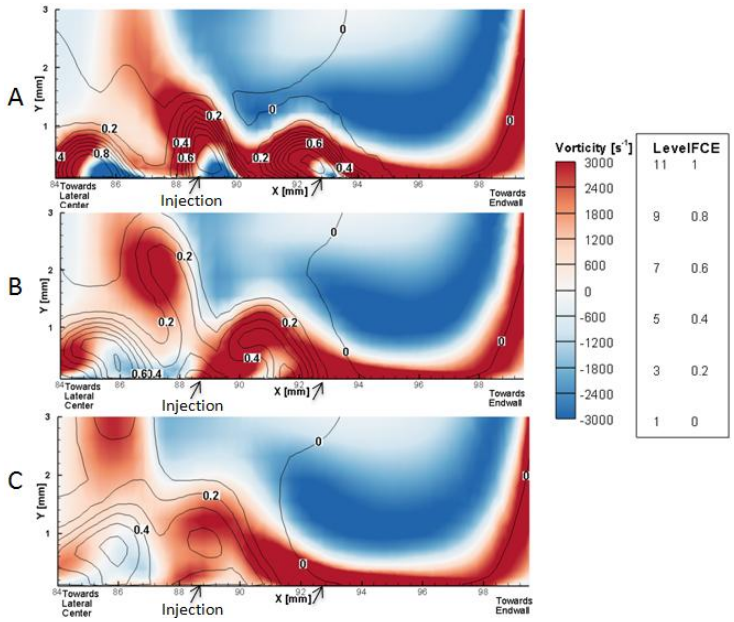

Figure 25: Development of film cooling vortices and film cooling effectiveness distribution downstream from the injection hole with endwall effects for BR =1 and DR = 1.

It can be observed in Figure 25, that immediately the closest injection hole, noted by the arrow, the film coolant CRVP is greatly suppressed by the passage vortex. The next two closest film cooling holes are affected but not as strongly. As the passage vortex and film cooling CRVP move downstream, the passage vortex held its strength and film coolant is displaced away from the endwall. Also due to the secondary flow of the passage vortex, the coolant is lifted from the blade surface and carried away from the endwall in Location C. The film Coolant as no effect near the endwall and the thermal impact of the film coolant is less prominent farther and farther from the endwall as the location moves farther from the injection location.

Compound Angle Effects

The following section will explain how the variance of the compound angle effects the development of the film cooling vortices in conjunction with the endwall passage vortex as well as the impacts that these compound angles have on the secondary losses. The images in Figure 26 show the development of coolant being injected from the 4^{th} Row on the Suction Side of the blade as shown in Table 7 with a Blowing Ratio and Density Ratio equal to 1. The top row on the image is with the smallest compound angle, 15.76°, the center row on the image is with the original compound angle, 19.70°, and the bottom row is with the largest compound angle 23.63°.

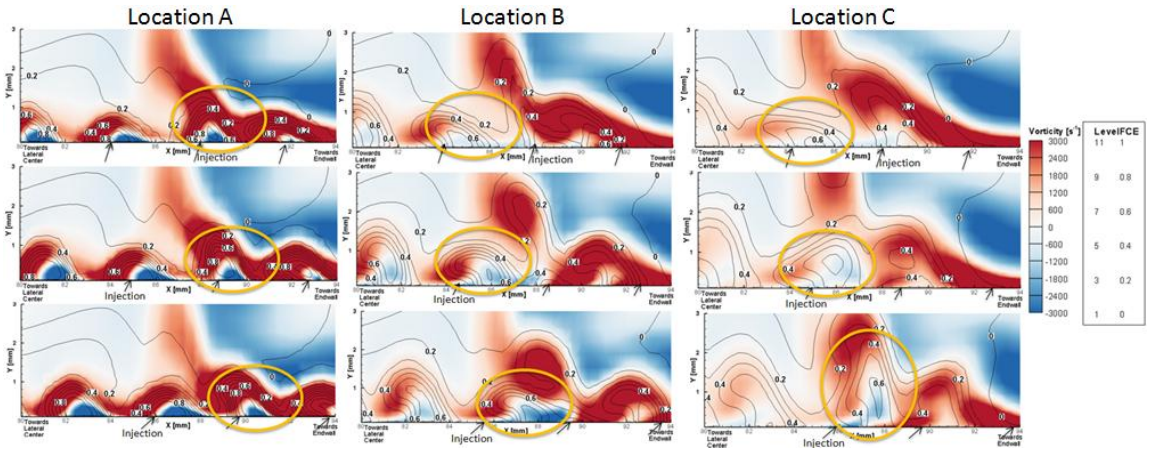

Figure 26: Development of film cooling vortices and FCE distribution from coolant injection holes with endwall effects for varying compound angle

The following table shows the compound angle injection for the three different cases.

Table 7: Film coolant compound angles for 3 different cases

	Original CA	Increased CA 20%	Decreased CA 20%
4th Row	19.70°	23.63°	15.76°
5th Row	22.78°	27.34°	18.23°
6th Row	25.86°	31.04°	20.69°

As seen in Figure 26 immediately from the injection location the film coolant with the highest compound angle (bottom) row is least affected by the passage vortex. The CRVP between two adjacent holes begin to interact right away as seen in the bottom right image. The vortices seem to connect between the two adjacent holes farther from the endwall. This is due to one of the injection holes being suppressed more with a

higher compound angle. With a higher compound angle, the CRVP is not immediately displaced and disrupted by the passage vortex with the same intensity as the low compound angle injection.

As the coolant vortices lose intensity in Location B, two coolant hole diameters downstream in the streamwise direction, the passage vortex begin to remove coolant from the immediate area. The CRVP in the small compound angle geometry stays close to the surface and moves away from the endwall rather hurriedly. With a high compound angle, the coolant lifts off from the blade surface but is not displaced as far from the endwall when comparison to a low compound angle. When the coolant vortices are studied at Location C, 4 coolant hole diameters downstream, it can be noted that the coolant lifts-off from the blade surface more as the compound angle increases. This is distinguished in Figure 26 through the golden circles showing the same coolant hole vortex development. This liftoff increases with the increase compound angle because more coolant momentum is directed counter to the flow direction of the passage vortex (a blue coolant vortex versus the red passage vortex). This opposite direction of coolant momentum with weakening vortex strength is going to allow for the passage vortex to lift the coolant away from the blade surface, still leaving the passage vortex region unprotected from the high thermal loads. Thus, the lateral displacement of film coolant is the same for all three compound angles but there is more liftoff with a higher compound injection angle because the passage vortex strength is much larger than the CRVP strength.

Although the compound angle does not have significant impact on the lateral spreading of coolant in the near wall region, the introduction of coolant with a larger compound angle actually has negative drawbacks. The secondary losses defined below increase with the introduction of a larger compound angle film cooling.

$$\zeta = \frac{P_{tot,in} - P_{tot,exit}}{P_{tot,in} - P_{s,in}} \tag{17}$$

Figure 27 shows the contour Plot of the Secondary Flow Losses at the Trailing Edge of the Blade Channel for the three different compound angle injections. The left side of each contour plot is the pressure side of the channel and the right side of the plot is the suction side of the channel.

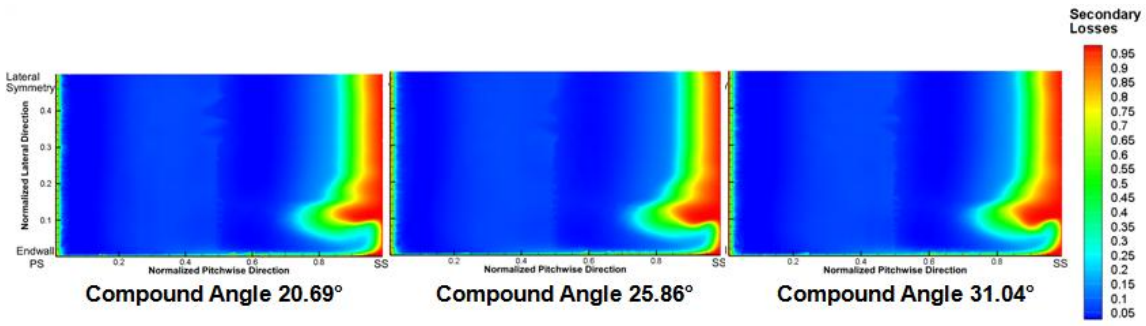

Figure 27: Contour plot of secondary losses at the trailing edge of the turbine blade subjected to film cooling with varying compound angles

The passage vortex is clearly seen in these images of secondary losses as the large loss bubble that is near the endwall of the blade channel. This passage vortex is significant on the suction side of the blade as opposed to the pressure side of the blade due to the difference in pressure across the channel. The film coolant being injected into

the system actually moves the passage vortex off the endwall with a zone of no losses close to the endwall. This is due to the injection of flow in a direction different from the mainstream flow. As the compound angle increases, the passage vortex losses actually grow. This growth of losses is seen through a protrusion growth the secondary loss bubble. These additional losses make sense as more coolant is injected in a direction different from the mainstream resulting in more secondary flow. For the turbine blade channel, adding coolant with a higher compound angle is less beneficial to the turbine performance and no benefits in coolant performance occurs in the near endwall region.

Density Ratio Effects

The Density Ratio is another parameter that is varied in this study. When the Density Ratio is higher, the temperature difference between the coolant and mainstream fluid becomes larger due to the density variation with termpature. As the mainstream temperature is 300 K when the Density Ratio is 1.25 and 1.50 the corresponding temperatures were 288.33 K and 233.33 K, respectively. For all Density Ratio varying cases, the Blowing Ratio was held constant at 1 giving the same coolant momentum in all cases. This constant coolant momentum resulted in no change in the CRVP intensity and shape. Figure 28, shows the development of the film cooling vortices and distribution of film coolant for the three different Density Ratios studied.

The shape, location, and magnitude of vorticity of the film cooling vortices does not change when varying the Density Ratios. All of the vorticity interactions between the

film coolant and the passage vortex is the exact same. The only differences that exists are the difference in magnitude of the film cooling effectivness

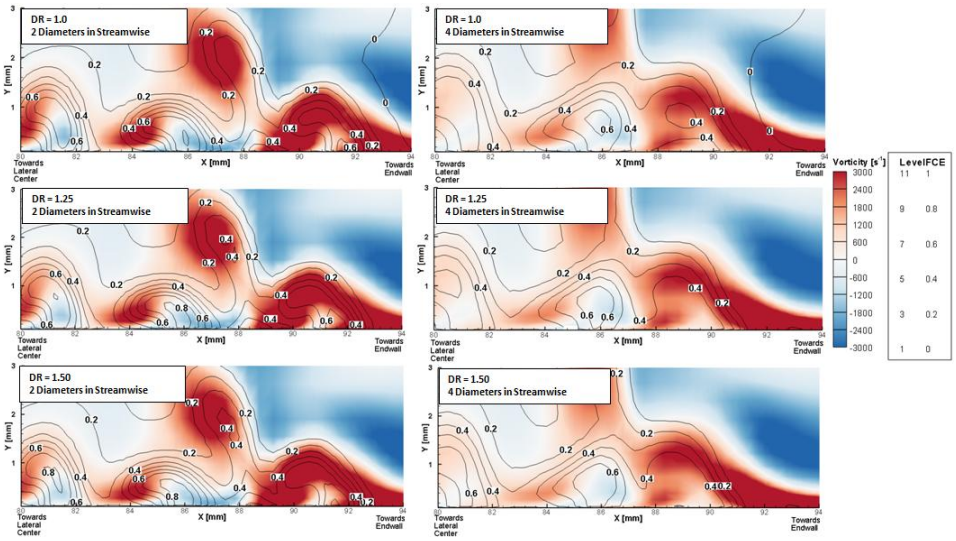

Figure 28: Development of film cooling vortices and FCE distribution from coolant injection holes with endwall effects for varying density ratios

In Figure 28, the vorticity is the same at both 2 diameters downstream and 4 diameters downstream for all three Density Ratios. However, within those vortices the magnitude of the film cooling effectiveness is higher. This is due to the thermal gas entrainment. With a larger temperature difference, at higher Density Ratios the coolant entrainment increases resulting in a higher local film cooling effectiveness. Even though, the local film cooling effectiveness increases with a higher Density Ratio, the displacement of the coolant way from the endwall is the same in any case.

Blowing Ratio Effects

The last parameter varied in this study was the Blowing Ratio. The Blowing Ratio was varied between 0.5 and 1.5 at a Density Ratio of 1, so the coolant velocity was varied in the different cases. Varying this coolant velocity resulted in different coolant momentum strength. Figure 29 displays the difference in the film cooling vortices interacting with the passage vortex for a Blowing Ratio of 0.5 (top) row, 1.0 (middle row) and 1.5 (bottom row) at locations of 2 coolant hole diameters and 4 coolant hole diameters downstream of 4th row injection on the suction surface of the blade near the endwall.

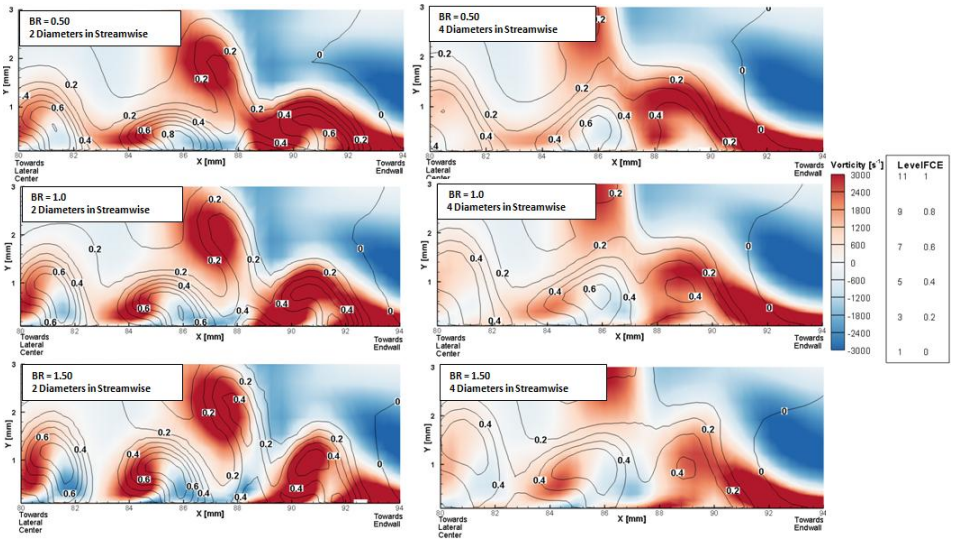

Figure 29: of Film cooling vortices and FCE distribution from coolant injection holes with endwall effects for varying blowing ratios

The three different Blowing Ratios studied in Figure 29 give insight on how with a higher Blowing Ratio, the shape and interaction between film cooling vortices and the passage vortex differ. With a higher Blowing Ratio, the CRVP has a higher strength and more liftoff. This lift-off is apparent in comparing the CRVP between the BR = 0.5 and the BR = 1.5 two diameters downstream of injection. With a higher Blowing Ratio, the Film Cooling Vortex is larger in size while with a low Blowing Ratio the Film Cooling Vortex is suppressed towards the surface. This is because with a low Blowing Ratio the momentum of the coolant injected is not large enough to penetrate the momentum of the mainstream fluid. This momentum deficit in low Blowing Ratio cases results in film cooling thermal performance staying low to the blade surface and having minimal downstream impact.

With a variance in Blowing Ratio, the Film Cooling Effectiveness there is no change in the impingement of coolant into the passage vortex. The local strength of the film cooling effectiveness is larger but the passage vortex still displacement the coolant with the same magnitude. Again, the momentum of the coolant is not as strong as the momentum of the secondary flow but coolant entrainment is strong resulting in a high film cooling effectiveness with a high Blowing Ratio. Ultimately, the Blowing Ratio does not have any immediate effect on the region near the endwall due to the strength of the passage vortex.

Overall Film Cooling Effectiveness on Blade Suction Side

The following section explains the overall film cooling effectiveness on the suction side of the blade surface. This section is going to show how changing the parameters effects the local film cooling effectiveness and to see if changing these parameters has any effect on penetrating the passage vortex region near the endwall. Figure 30, Figure 31, and Figure 32 show the local film cooling effectiveness contour plots for the variance of the three different parameters on the suction side of the blade. The figures capture from the 4th Row injection, S/S_o = 0.48 to the trailing edge of the blade, S/S_o = 1.0 and from the endwall to a lateral distance of 70 mm away from the endwall to capture the compound angles.

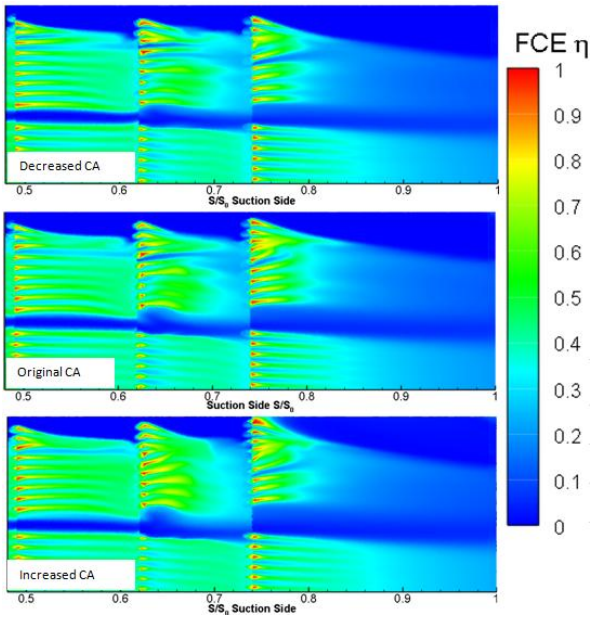

Figure 30: Film cooling effectiveness contour plot of the suction side of the blade from the 4th row (S/So =0.48) to the trailing edge (S/So = 1) with varying film cooling compound angles

In Figure 30 different compound angle injection film cooling effectiveness contour plots are shown. It is seen in this figure that the film cooling effectiveness magnitude is not affected at all by the compound angle. With a larger compound angle there is slightly more spreading immediately but once the film coolant reaches a few hole diameters downstream the effects of the variance in compound angle injection is completely negligible. With a larger compound angle the holes are located closer to the endwall as seen in the image but the passage vortex carries the same shape of the coolant displacement downstream from the hole location. It can be concluded that changing the compound angle has no effect on the film cooling effectiveness in the endwall region due to the high vorticity of the passage vortex compared to that of the film cooling vortices.

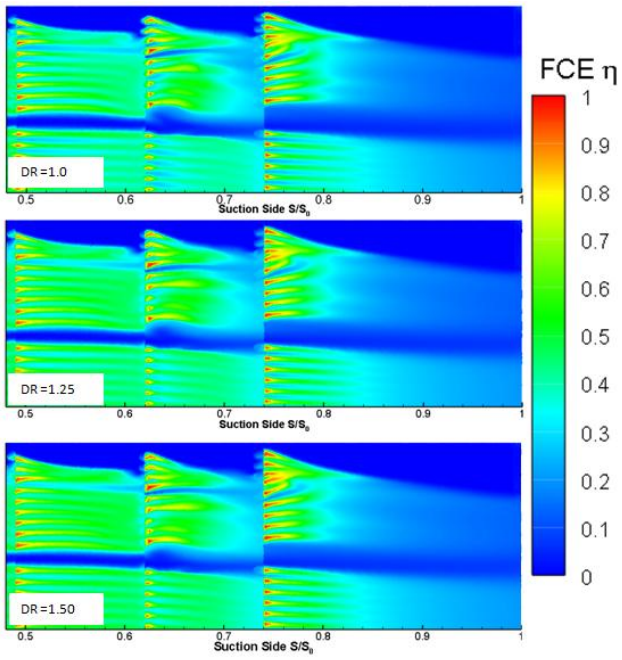

Figure 31: Film cooling effectiveness contour plot of the suction side of the blade from the 4th row (S/So =0.48) to the trailing edge (S/So = 1) with varying film cooling density ratio

By increasing the Density Ratio, as seen in Figure 31, only the local film cooling effectiveness is increased. This same effect was seen in the film cooling vortices development in respect to Density Ratio earlier in the chapter. No changes in shape occur in the passage vortex region and near wall region only a slightly increased local effectiveness. Again, the passage vortex completely displaces the film coolant and the coolant momentum is much smaller than the momentum and vorticity of the passage vortex.

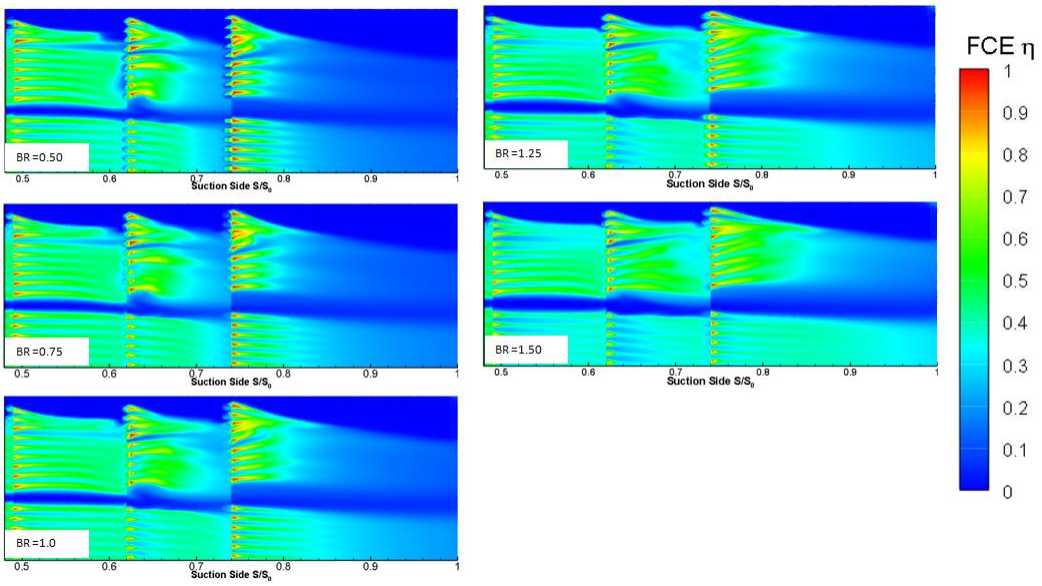

Figure 32: Film cooling effectiveness contour plot of the suction side of the blade from the 4th row (S/So =0.48) to the trailing edge (S/So = 1) with varying film cooling blowing ratios

By varying the Blowing Ratio, Figure 32, the passage vortex removes coolant at the same rate regardless of the Blowing Ratio. Due to the increased momentum of the film coolant with a higher Blowing Ratio, the film coolant is going to protect the blade surface more, downstream of the injection holes. In addition, there is going to be more lift-off to the coolant from the blade surface with reattachment farther downstream with a higher Blowing Ratio. Especially in a higher convex curvature of the blade, such as the 4^{th} row at S/S_o = 0.5 the reattachment and interaction of the coolant occurs high downstream in the no compound angle region. Although there is more lift off from the blade surface, the passage vortex is still much stronger than the film cooling vortices and the displacement from the endwall is the same magnitude regardless of the Blowing

Ratio. The passage vortex removes coolant from the endwall region with the same intensity for all Blowing Ratios.

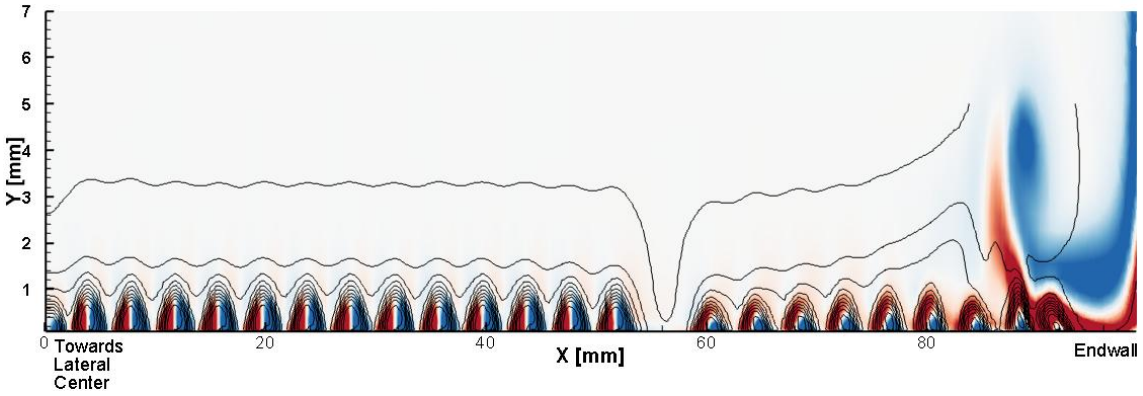

Figure 33: Passage vortex and film cooling vortices distributed laterally across half of the blade surface with corresponding FCE lines

The overall size and magnitude of the Passage Vortex is much larger than that of the film cooling CRVP. Figure 33 shows the vorticity magnitude and film cooling effectiveness from the lateral midspan to the endwall of the blade immediately after coolant is injected from the 4th Row on the Suction Side. The Passage Vortex on the endwall is much larger in size than that of the film cooling CRVP. With the passage vortex having high vorticity 8 mm from the blade surface and 15 mm blade endwall. This passage vortex size is much larger than the 2 mm height and 4 mm width of that from the film cooling CRVP. In addition, the magnitude of the vorticity does not dissipate in the passage vortex as it does in the CRVP. As the CRVP vorticity decreases

downstream from the injection hole, the passage vortex will displace the coolant away from the endwall.

As seen in this study, despite varying the compound angle, Density Ratio, and Blowing Ratio of coolant injection, the passage vortex is going to displace coolant near the endwall because of the higher vorticity intensity of the passage vortex compared to that of the film cooling Counterrotating Vortex Pair.

CHAPTER VI

CONCLUSIONS

To improve the performance and efficiency of a Gas Turbine cooling methods have been introduced to the turbine blades in order to protect the blades from high thermal stresses. One of the cooling methods that has been introduced over the past decades is film cooling, a method in which a secondary fluid is injected from the turbine blade at discrete hole locations to act as a protective layer to reduce the thermal load on the blade. However, with film cooling, turbine blades are susceptible to large vortices on near the endwall on the suction side of the blade due to the development of horseshoe and passage vortices in the blade channel and these vortices are known to produce high heat transfer coefficients in this region as well as displace any film coolant in this region.

This investigation studied the near film injection flow region of a low pressure turbine blade subjected to film cooling in conjunction with the development of endwall vortices that develop along the suction side of a turbine blade. By performing a numerical analysis using ANSYS CFX, a macroscopic evaluation of aerodynamic and heat transfer properties were made in comparison to an experimental benchmark with film coolant injection with a Density Ratio and Blowing Ratio equal to 1.

This study showed good agreement with overall trends of coefficient of pressure distribution, separation bubble development, Nusselt Number distribution, and Film Cooling Effectiveness distribution. However, Velocity Fluctuations were over predicted near the blade surface in the boundary layer for the RANS CFD Models, this over

predicted of velocity fluctuation resulted in a higher mass, momentum, and energy transfer in this boundary layer region, resulting in a difference in magnitude of the Separation Bubble, Nusselt Number, Film Cooling Effectiveness. This error in predicting the Reynolds Stress Tensor does not allow for adequate prediction of the Total Energy Equation in the boundary layer of the blade, developing the need for improvements of the turbulence models in high curvature geometries.

In this study, different parameters are varied to understand the effects that these parameters have on the film cooling Counterrotating Vortices in Conjunction with the Passage Vortex in the near endwall region of the suction surface of the blade. The three different parameters that were varied were the Coolant Compound Injection Angle, the Density Ratio, and the Blowing Ratio. It is concluded, with an increase in the compound injection angle the film cooling vortices lift-off due to the counteraction of the passage vortex. This lift-off is a result of immediate disturbance of the passage vortex at the point of introduction into the mainstream. By varying the Density Ratio, the film cooling vortex size, shape, and intensity did not change. The only effect that was seen when varying the Density Ratio was the increase in the local film cooling effectiveness magnitude. This increase in magnitude can be attributed to the larger difference in temperature between the mainstream and coolant fluid resulting in a more coolant entrainment. Lastly, by varying the Blowing Ratio, there is more coolant lift-off with a higher Blowing Ratio due to the increase in momentum. This increase in momentum in turn resulted in a higher local effectiveness.

Although there were some immediate differences in varying the three parameters in this study, one ultimate conclusion that may be made is that the passage vortex has a much higher vorticity and physical size than that of the film cooling vortices. As the film cooling vortices intensity dissipates quickly, downstream of the passage vortex is going to displace the coolant in the near endwall region immediately when coolant is introduced. The near endwall region is going to be unaffected by film coolant in any case due to the passage vortex size and intensity displacing the coolant introduced into the system for all cases.

REFERENCES

1. Breeze, P., *Gas-Turbine Power Generation*. 2016: Academic Press.
2. Schobeiri, M., *Turbomachinery Flow Physics and Dynamic Performance*. 2005: Springer.
3. Lakshminarayana, B., *Fluid Dynamics and Heat Transfer of Turbomachinery*. 1996: Wiley Online Library. 809.
4. Han, J.-C. and S. Ekkad, *Recent Development in Turbine Blade Film Cooling.* International Journal of Rotating Machinery, 2001. **7**(1): p. 21-40.
5. Fric, T. and A. Roshko, *Vortical Structure in the Wake of a Transverse Jet.* Journal of Fluid Mechanics, 1994. **279**: p. 1-47.
6. Pedersen, D., E. Eckert, and R. Goldstein, *Film Cooling with Large Density Diffferences Between the Mainstream and the Secondary Fluid Measured by the Heat-Mass Transfer Analogy.* ASME, Transactions, Series C-Journal of Heat Transfer, 1977. **99**: p. 620-627.
7. Goldstein, R. and E. Eckert, *Film Cooling of a Gas Turbine Blade.* Journal of Engineering for Power, 1978. **100**(3): p. 476-489.
8. Vinton, K.R., et al., *Combined Effects of Freestream Pressure Gradient and Density Ratio on the Film Cooling Effectiveness of Round and Shaped Holes on a Flat Plate. ASME*. Journal of Turbomachinery. 2017. 1**39**(4): p. 1223-1332.

9. Leylek, J.H. and R.D. Zerkle, *Discrete-Jet Film Cooling: A Comparison of Computational Results With Experiments.* ASME. Journal of Turbomachinery. 1993. 116(3): p. 358-368.

10. Ligrani, P., et al., *Film-Cooling From Holes With Compound Angle Orientations: Part 1—Results Downstream of Two Staggered Rows of Holes With 3d Spanwise Spacing.* Journal of Heat Transfer, 1994. **116**(2): p. 341-352.

11. Chowdhury, N.H.K., P.K. Dey, and F.E. Ames, *The Influence of Inlet Contraction on Vane Aerodynamic Losses and Secondary Flows With Variable Turbulence and Reynolds Number.* ASME. Turbo Expo: Power for Land, Sea, and Air, Volume 7: Turbomachinery, Pars A, B, and C. 2011 p. 741-750.

12. Goldstein, R. and R. Spores, *Turbulent Transport on the Endwall in the Region Between Adjacent Turbine Blades.* ASME Journal of Heat Transfer, 1988. **110**(4): p. 862-869.

13. Lynch, S.P., et al., *Computational Predictions of Heat Transfer and Film-Cooling for a Turbine Blade with Nonaxisymmetric Endwall Contouring.* Journal of Turbomachinery, 2011. **133**(4): p. 041003.

14. Sen, B., D.L. Schmidt, and D.G. Bogard, *Film Cooling With Compound Angle Holes: Heat Transfer.* ASME. Journal of Turbomachinery. 1996. **118**(4): p. 800-806.

15. Martinez, S., *Benchmarking of Computational Models against Experimental Data for Velocity Profile Effects on CFD Analysis of Adiabatic Film-Cooling*

Effectiveness for Large Spacing Compound Angle Full Coverage Film Cooling Arrays. McNair Scholars Research Journal, 2015. **2**(1): p. 1.

16. Berhe, M.K. and S.V. Patankar, *Curvature Effects on Discrete-Hole Film Cooling.* Journal of Turbomachinery, 1999. **121**(4): p. 781-791.
17. Mhetras, S. and J.-C. Han, *Effect of Unsteady Wake on Full Coverage Film-Cooling Effectiveness for a Gas Turbine Blade.* AIAA Paper No. AIAA-2006-3404, 2006.
18. Ling, Z., W. Guo-liang, and P. Tao. *Numerical Investigation on Two Compound Angles Film Cooling of Stator Blades*. in *Proceedings of the 2011 International Conference on Informatics, Cybernetics, and Computer Engineering (ICCE2011) November 19–20, 2011, Melbourne, Australia*. 2011. Springer.
19. Menter, F.R., *Two-Equation Eddy-Viscosity Turbulence Models for Engineering Applications.* AIAA Journal, 1994. **32**(8): p. 1598-1605.
20. Menter, F.R. *Trends and Challenges in Modelling Complex Turbulent Flows*. in *Proceedings of the 14th International Conference on Fluid Flow Technologies, Hungary*. 2009.
21. Spalart, P. and M. Shur, *On the Sensitization of Turbulence Models to Rotation and Curvature.* Aerospace Science and Technology, 1997. **1**(5): p. 297-302.
22. auf dem Kampe, T., et al., *Experimental and Numerical Investigation of Flow Field and Downstream Surface Temperatures of Cylindrical and Diffuser Shaped Film Cooling Holes1.* Journal of Turbomachinery, 2013. **135**(1): p. 011026.

23. Lakehal, D., *Near-Wall Modeling of Turbulent Convective Heat Transport in Film Cooling of Turbine Blades With the Aid of Direct Numerical Simulation Data*. Journal of Turbomachinery, 2002. **124**(3): p. 485-498.

24. Bergeles, G., A. Gosman, and B. Launder, *The Turbulent Jet in a Cross Stream at Low Injection Rates: a Three-Dimensional Numerical Treatment.* Numerical Heat Transfer, Part A: Applications, 1978. **1**(2): p. 217-242.

25. Medic, G. and P.A. Durbin, *Toward Improved Film Cooling Prediction.* Journal of Turbomachinery, 2002. **124**(2): p. 193-199.

26. Germain, T., M. Nagel, and R. Baier. *Visualisation and Quantification of Secondary Flows: Application to Turbine Bladings With 3D-Endwalls*. in *Paper ISAIF8-0098, Proc. of the 8th Int. Symposium on Experimental and Computational Aerothermodynamics of Internal Flows, Lyon*. 2007.

27. Alameldin, A., et al. *CFD Analysis of Suction and Pressure Side Film Cooling Influence on Vane Aero Performance in a Transonic Annular Cascade*. in *ASME Turbo Expo 2014: Turbine Technical Conference and Exposition*. 2014. American Society of Mechanical Engineers.

28. Laskowski, G.M., A.K. Tolpadi, and M.C. Ostrowski. *Heat transfer predictions of film cooled stationary turbine airfoils*. in *ASME Turbo Expo 2007: Power for Land, Sea, and Air*. 2007. American Society of Mechanical Engineers.

29. Hylton, L., et al., *The Effects of Leading Edge and Downstream Film Cooling on Turbine Vane Heat Transfer.* Final Report General Motors Corp., Indianapolis, IN. ALlision Gas Turbine Div. 1. 1988.

30. Nikparto, A. and M.T. Schobeiri. *Experimental Investigation of Film Cooling Effectiveness of a Highly Loaded Turbine Blade Under Steady and Periodic Unsteady Flow Conditions*. in *ASME Turbo Expo 2016: Turbomachinery Technical Conference and Exposition*. 2016. American Society of Mechanical Engineers.

31. Öztürk, B., M. Schobeiri, and D.E. Ashpis. *Intermittent Behavior of the Separated Boundary Layer Along the Suction Surface of a Low Pressure Turbine Blade Under Periodic Unsteady Flow Conditions*. in *ASME Turbo Expo 2005: Power for Land, Sea, and Air*. 2005. American Society of Mechanical Engineers.

32. Ansys, C., *ANSYS CFX-solver theory guide.* ANSYS CFX Release, 2012. **11**: p. 69-118.

33. Nikparto, A. and M.T. Schobeiri. *Numerical and Experimental Investigation of Aerodynamics on Flow Around a Highly Loaded Low-Pressure Turbine Blade With Flow Separation Under Steady and Periodic Unsteady Inlet Flow Condition*. in *ASME Turbo Expo 2016: Turbomachinery Technical Conference and Exposition*. 2016. American Society of Mechanical Engineers.